Nano Research

ISSN 1998-0124 CN 11-5974/O4
https://doi.org/10.1007/s12274-023-6006-2

Review Article

Aligned carbon nanotubes for lithium-ion batteries: A review

Chinaza E. Nwanno and Wenzhi Li (✉)

Department of Physics, Florida International University, Miami, FL 33199, USA

Received: 7 April 2023 / **Revised:** 6 July 2023 / **Accepted:** 16 July 2023

ABSTRACT

Nanoscale materials are gaining massive attention in recent years due to their potential to alleviate the present electrochemical electrode constraints. Possessing high conductivity (both thermally and electrically), high chemical and electrochemical stability, exceptional mechanical strength and flexibility, high specific surface area, large charge storage capacity, and excellent ion-adsorption, carbon nanotubes (CNTs) remain one of the most researched of other nanoscale materials for electrochemical energy storage. Rather than having them packed at random, CNTs perform better when packed/grown to order, vertically or horizontally aligned to a substrate. This study presents an overview of the impact of CNT alignment on the electrochemical performance of lithium-ion batteries (LIBs). The unique properties of vertically aligned CNTs (VACNTs) for LIB application were discussed. Furthermore, the mechanisms of charge storage and electrochemical performances in VACNT-based (pristine and composites) anodes and cathodes of LIBs were succinctly reviewed. In the end, the existing challenges and future directions in the field were also briefly discussed.

KEYWORDS

nanoscale, vertically aligned carbon nanotubes (VACNTs), composites, lithium-ion batteries (LIBs), anodes, cathodes

1 Introduction

The ever-increasing global energy demand and the rapid proliferation of miniaturized electronic devices have positioned nanotechnology at the forefront of modern-day research in material science and engineering, offering the possibility of synthesizing materials with nanoscale dimensions and unique properties different from their bulk counterparts [1]. Regarding lithium-ion-batteries (LIBs), these unique properties have led to the development of batteries with greatly improved electrochemical performance [2]. Compared to bulk electrodes, nanostructured electrodes offer reduced distances for ionic and electronic transport owing to their greatly reduced sizes and increased area-to-volume ratio [3]. This has resulted in batteries with higher specific energy capacities and excellent rate capabilities [4]. Furthermore, prolonged battery cycle life has been achieved by exploiting the structural stability of nanoscale electrode materials, as they are known to better accommodate the mechanical stress associated with lithiation and de-lithiation during the cycling process [5].

Several nanoscale electrode materials have been explored by researchers in different attempts to improve the electrochemical performance of state-of-the-art LIBs, with varying degrees of success [6–18]. Among such materials are carbon nanotubes (CNTs) [19–22], which are one-dimensional (1D) cylinders of graphene sheets. This unique structure of CNTs endows them with exceptional properties such as superb electrical and thermal conductivities, exceptional mechanical strength and flexibility, and high chemical and electrochemical stability, which are desirable for battery applications [23–25]. However, the vertically aligned carbon nanotubes (VACNTs), which consist of arrays of individual CNTs aligned perpendicular to the substrate surface, have been touted to be a more suitable electrode structure for energy storage devices such as supercapacitors [26, 27] and LIBs [28, 29]. Compared to their randomly oriented counterparts, the VACNTs offer higher mechanical strength, larger surface areas, and greatly enhanced electrolytic access to the electrode [30, 31]. For instance, it was clearly pointed out that the large surface area and the vertical conducting channel of VACNTs are the reasons for the exceptional power density and rate capability delivered by the electrode fabricated by using VACNTs grown on activated reduced graphene oxide (VACNTs on a-rGO) [32]. Studies have also demonstrated that the VACNT electrode architecture ensures proper attachment of individual CNTs to the current collector due to their high degree of alignment, giving rise to greatly improved electronic transport and ionic diffusion [33–35].

VACNTs have also been incorporated into other electrochemically active materials, including graphene, metals, and metal oxides, to form composite electrodes [36]. Such a system combines the exceptional intrinsic properties of the VACNTs and the high specific capacity of the active materials. Silicon, for instance, has emerged as a promising alternative anode material because of its high theoretical specific capacity of 4200 $mAh \cdot g^{-1}$ and relatively huge abundance in nature [37]. However, its use has been hindered by pulverization linked to its large volumetric expansion and contraction during charge and discharge cycles. This colossal electrode damage seen in Si and other active materials has been circumvented by exploiting the high mechanical strength and the mesoporous nature of the VACNTs by several researchers [38–43]. In addition to this, the VACNTs also improve the electronic conductivity of the host materials owing to their high anisotropic conductivity along the axial direction [44].

Address correspondence to Wenzhi.Li@fiu.edu

VACNTs have also been used to improve the electrochemical performance of the existing LIB cathode materials. The VACNTs provide regular pore structures with large surface areas for the uniform deposition of increased mass of electroactive cathode materials capable of achieving high energy and power densities. They are also used as conductive networks or additives to enhance the electronic transport in the poorly conductive cathode electroactive materials, giving rise to excellent rate capabilities.

While several reviews have been carried out on the methods of synthesis [30, 45], growth techniques and mechanisms [46, 47], properties [48], alignment methods [49], and large-scale production of VACNTs [50], no thorough review, to the best of our knowledge, has been done on the effect of alignment on the electrochemical performance of VACNTs and their composites in LIBs. Thus, this review aims to elucidate the electrochemical performance of VACNTs and VACNTs-based composites as both anode and cathode materials for LIBs.

2 Nanoscale materials and their benefits as electrode materials for LIBs

With dimensions in the order of 100 nm or smaller, nanoscale materials have gained massive attention in modern-day research. As the size of a particle approaches the nanoscale range, its boundary conditions are destroyed, and the particle surface is changed, resulting in properties that are different from those of their bulk counterparts [51]. For example, the yellow color of bulk Au solution changes to red at the nanoscale level [52]. Meanwhile, the ability to alter the properties of materials at the nanoscale level has resulted in materials with some unique features, such as increased surface areas [53], improved magnetic behavior [54], exceptional thermal and electrical conductivities [55], pronounced quantum effects [56], and excellent mechanical properties [57].

These features have placed nanomaterials at the forefront of scientific research, and in recent years, they have found applications in a number of fields, such as drug delivery [58–61], energy storage [62–65], electrocatalysis [66–69], biosensing [70–73], and water purification [74–77].

In LIBs, the small size of nanomaterials shortens the transport paths of electrons and Li^+ ions, thereby enhancing the rate capability and cyclability of the battery [1]. More so, these materials can withstand the large strain associated with lithium insertion during charge and discharge process, which could lead to pulverization and hence, a huge capacity loss [5]. For instance, the large volume expansion that occurs in bulk Si electrodes has been mitigated by replacing them with their nanostructured counterparts, resulting in an improved cyclability [37, 78–80]. In addition, the large surface area possessed by nanoscale electrodes lowers the charge transfer resistance by improving the electrode–electrolyte contact. This increases the rate at which Li^+ ions move in and out of the electrode from the electrolyte and back. The large surface area also increases the energy density of the battery by allowing more Li^+ ions to be intercalated into the electrode material. However, this property has been reported to increase surface reactions, which leads to irreversible lithium loss (decreased reversible capacity) upon initial cycling [2].

Furthermore, conventional LIBs can also profit a lot from the ability of these nanoscale materials to be used in manufacturing electrodes of various sizes, shapes, or forms, enabling their incorporation into functional architectures [3]. For example, the huge battery packs, which are usually seen as separate components in electric vehicles, can be incorporated into the vehicle framework instead of occupying unnecessary space elsewhere and consequently adding dead weight to the entire structure. This also opens the door for LIBs to be used in manufacturing portable and flexible electronics (including wearable, foldable, and stretchable devices), which are in increasing demand. Instead of the old-fashioned bulky coin cells, miniaturized stretchable cells could be incorporated into these devices. The above-discussed benefits and disadvantages are further summarized in Table 1 for easier comprehension.

Figure 1 illustrates some of the carbon-based nanoscale and nanostructured materials that have been studied in recent years as prospective LIB electrode materials. However, this review will focus on CNTs, specifically the vertically aligned ones. The general structures and properties of CNTs as well as their method of alignment are discussed briefly in the subsequent sub-sections.

2.1 Structures and properties of CNTs

CNTs are a special kind of nanoscale material. They are 1D cylinders of graphene sheets. Subject to the number of walls that the tube is made of, CNTs can be structurally divided into single-walled CNTs (SWCNTs, for CNTs having a single tube wall) and multi-walled CNTs (MWCNTs, for CNTs containing more than a single tube wall), as can be seen in Fig. 2(a). Comparatively, the diameter of SWCNTs is roughly 1 nm, while that of MWCNTs is in the range of 3–30 nm [83] or much larger, with an interlayer distance of 0.34 nm between neighboring graphene sheets [84]. Furthermore, the structural description of SWCNT is governed by the geometric ordering (chirality) of the carbon atoms at the rim of the tube (Fig. 2(b)) [85], and is defined by the chiral vector ($\boldsymbol{n}$, $\boldsymbol{m}$) [86–88]. For equal values of the chiral vector (i.e., $n = m$), the SWCNT is termed armchair, while zigzag SWCNTs are the ones having the values of m equal to zero ($m = 0$), and lastly, the chiral SWCNTs have different values of n and m ($n \neq m$).

The unique structure of CNTs endows them with exceptional electrical, mechanical, thermal, and electrochemical properties. The 1D structure of CNTs enables a ballistic transport of electrons in CNTs, giving them the ability to convey electrons over long lengths with little (due to defects) or no interruptions, making CNTs more electrically conductive than copper [90, 91]. However, the electrical properties of CNTs are significantly influenced by their chirality and diameter of the nanotubes [92]. SWCNTs can either be metallic or semi-conductive, depending on the values of

Table 1 Summary of the various advantages and disadvantages of nanomaterials in lithium-ion battery application

Advantages	Disadvantages
(1) Enhanced rate capability and cyclability due to the reduced transport distances for both electrons and Li^+ ions [2].	(1) Increased side reactions due the large surface area of the nanoscale materials [3].
(2) Higher specific capacity and improved electrode–electrolyte contact area as a result of the larger surface area possessed by the nanoscale materials [3].	(2) Nanoscale materials are difficult to synthesize and their dimensions are hard to control [2].
(3) Improved structural stability and Coulombic efficiency (CE) resulting from the ability of the nanoscale materials to withstand the strain associated with the volumetric change during lithium insertion and extraction [81].	(3) Low volumetric energy density resulting from the reduced mass of the nanoscale materials [2].
(4) They allow for new lithium storage mechanisms that are not possible with bulk materials such as the conversions reactions associated with nanostructured metal oxides, sulfides, nitrides, and fluorides [82].	

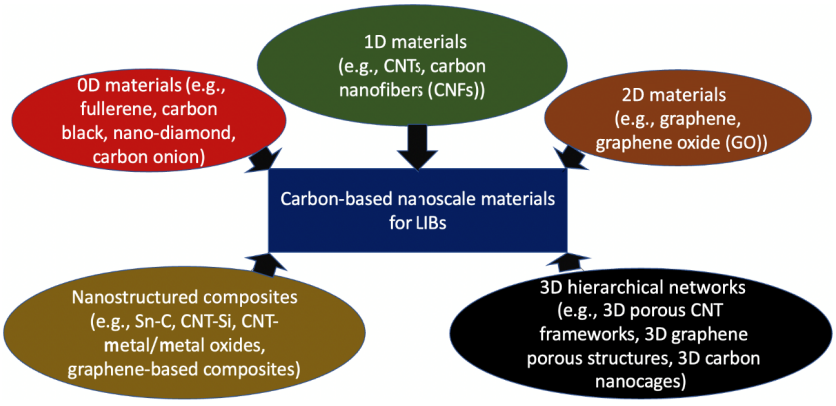

Figure 1 Classifications of carbon-based nanoscale materials used as electrode materials for LIBs.

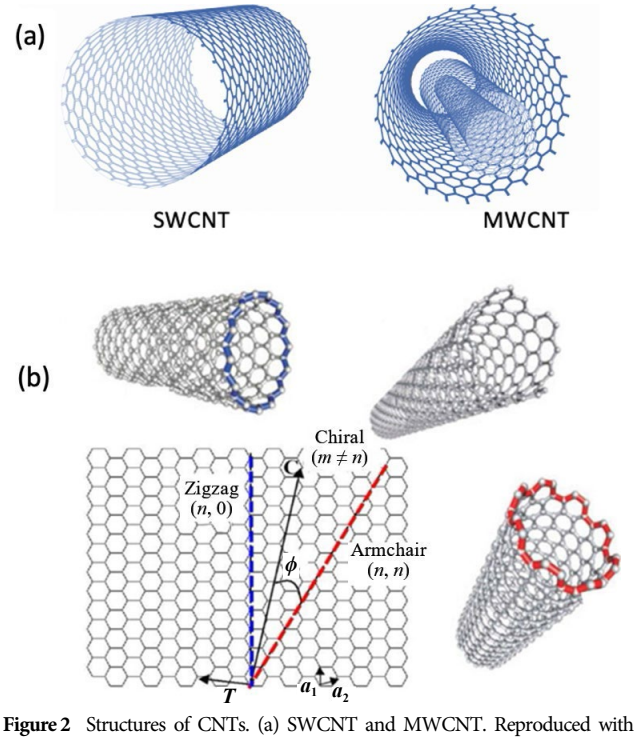

Figure 2 Structures of CNTs. (a) SWCNT and MWCNT. Reproduced with permission from Ref. [89], © Devi, R. et al. 2021. (b) Chirality of SWCNTs. Reproduced with permission from Ref. [85], © Tilmaciu and Morris 2015.

their chiral vector. The armchair SWCNTs are metallic (i.e., $n = m$), while SWCNTs with $n - m$ as a multiple of 3 are semi-conductive with a little bandgap; else, it is a moderate semi-conductor. However, with an increasing diameter or crystallite size, the bandgap from chirality decreases [93]. That is, nanotubes with larger diameters tend to be metallic, not minding their chirality. Like the SWCNTs, the electrical properties of MWCNTs can either be semi-conductive or metallic. However, the outer walls are dominantly metallic due to their larger diameter and physical contact with the conducting external electrode [94].

Furthermore, CNTs exhibit thermal conductivity twice that of the best thermal conductor (diamond) [23]. Experimentally, MWCNTs have shown thermal conductivity of 3500 $W \cdot m^{-1} \cdot K^{-1}$ at room temperature. Mechanically, CNTs have excellent values for Young's modulus (1002 GPa) and tensile strength (about 300 GPa), making them the strongest and stiffest materials ever known, thanks to the sp^2 bonds between the individual carbon atoms of the CNTs [23, 90, 95, 96]. Also, CNTs are very elastic; they can be bent, twisted, and kinked without fracture.

Although studies have shown that CNTs exhibiting these exceptional and desirable properties are outstanding candidates in several areas of application, such as energy storage, wearable electronics, chemical sensors, water filtration, and optoelectronics, there is still a large gap between what is predicted theoretically and what has been achieved experimentally [97]. As a result, researchers have delved into several ways of practically realizing the exceptional properties of CNTs. Ways such as functionalization, structural manipulations, compositing, and novel methods of synthesizing have all been explored [91, 95, 98]. All these strategies have been shown to be effective in improving and practically realizing the properties of CNTs. However, the impact of alignment on the electrochemical performance of CNTs in LIBs is the focus of this article, as there is still a dearth of review in this field.

2.2 CNT alignment

The properties of CNTs are anisotropic in nature, implying that CNTs exhibit different values of the same property when measured along different orientations [23, 99]. For instance, the experimentally obtained value of the Young's modulus of SWCNTs along the tube axis is 1002 GPa, while that obtained along the radial axis is far lesser [100], indicating that CNTs are softer in the radial direction than the tube axis [101]. However, an effective way of preserving the anisotropic properties of CNTs is by synthesizing them with uniform orientation—aligning. Studies have shown that aligning CNTs in a uniform direction not only facilitates their integration into physical devices but also significantly improves their desirable intrinsic properties [99, 102–107]. For instance, the work of Mei et al. on the morphological and microstructural comparison of aligned and bulk chemical vapor deposition (CVD)-grown CNTs showed that aligned CNTs exhibit higher purity and degree of graphitization than their unaligned counterpart [108]. Furthermore, the scanning electron microscopy (SEM) study of the materials revealed that unaligned CNTs tend to agglomerate in the absence of external forces while aligned CNTs retained their structure. Also, Chen recently investigated the effect of alignment on the thermal conductivity of CNT films and CNT fibers. The author concluded that CNT fibers were better thermal conductors than CNT films, which was attributed to a higher degree of alignment of CNT fibers than films [109]. By simply aligning the tubes, Ishikawa et al. were able to improve the electron mobility of SWCNT based thin film transistors from 30 $cm^2 \cdot V^{-1} \cdot s^{-1}$ in a previously reported work [110] to a whooping 1300 $cm^2 \cdot V^{-1} \cdot s^{-1}$ [111].

CNT alignment simply means the act of orienting individual CNTs of a CNT ensemble in the same direction. This makes it possible for the structural manipulation of each of the individual CNTs of the ensemble, as it would contain isolated straight individual CNTs [99], resulting in improved performance compared to unaligned/bulk CNTs. The alignment of CNTs can be done either perpendicular or parallel to the substrates. CNTs aligned perpendicular to the substrates are the VACNTs, while

CNTs aligned parallel to the substrates are referred to as horizontally aligned carbon nanotubes (HACNTs) [112]. However, there is a special kind of VACNTs, called super-aligned carbon nanotubes (SACNTs). They possess a higher degree of alignment, which stems from their thinner diameter and higher nucleation density [113]. Another distinguishing factor of SACNTs from VACNTs, aside from the degree of alignment, is the capability of the SACNTs to be converted into continuous films or yarns in their solid-state [114].

CNT alignment can be achieved either *in-situ* (during CNT growth) or *ex-situ* (post-CNT growth). Either way, there is a need for a driving force to incite the alignment process. The force can be generated by exposing them to external fields such as magnetic field, electric field, or shear field, or can be induced by conditions and limitations of the surrounding medium and substance, in the case of van der Waals interactions [112, 115, 116], as demonstrated in Fig. 3 below. For a deeper understanding of the mechanism of CNTs alignment and other aspects regarding the alignment of CNTs, the works of Refs. [30, 112, 115–120] are of good fit.

While HACNTs are more suitable for microelectronics by virtue of their direction of alignment, VACNTs have found applications in myriads of fields, such as the solar cells [121], biomedicine (e.g., biosensing, drug delivery, cell stimulation, regenerative medicine, and biomolecule filtration systems) [122], energy storage devices (e.g., LIBs and supercapacitors) [30, 31], black-body absorption [123], portable, flexible, and wearable electronic devices [124], as a result of their exceptional properties which would be discussed later in this review.

2.3 The conventional LIBs and their electrode limitations

The oil crisis of the 1960s and 1970s and the global pursuit for sustainable energy systems motivated scientists to research potential electrochemical energy storage devices that could store much more energies than the already existing ones. The earlier works of 2019 Chemistry Noble prize winners, Stanley Whittingham, John Goodenough, and Akira Yoshino [125], laid the foundation for the development of LIBs, culminating in the eventual commercialization of the first-ever LIBs by Sony in 1991 [126]. The modern-day rechargeable LIBs find applications in our day-to-day life, such as smartwatches, personal digital assistants (PDAs), mobile phones, laptops, drones, medical devices, power tools, and most recently, electrical vehicles. Compared to other rechargeable battery systems, such as Ni-Cd and Ni-metal hydride batteries, LIBs offer higher energy density with minimized volumetric and mass constraints, a broader range of temperature, minimal self-discharge rate, and no memory effect (lazy battery effect) [127].

Ever since its commercialization, the LIBs have remained at the forefront of the rechargeable batteries [128]. However, the performance (energy density, power density, safety, and rate capacity) of the present-day LIBs is still limited by the poor properties of the presently used electrode materials; thus, there is a need to develop advanced nanostructured electrode materials that can potentially address the present performance limitations of LIBs and ever-increasing energy demands.

The conventional LIBs consist of a graphite anode acting as the negative terminal, a lithium metal oxide cathode, such as lithium cobalt oxide ($LiCoO_2$ (LCO)), lithium manganese oxide spinel ($LiMn_2O_4$ (LMO)), and lithium iron phosphate olivine ($LiFePO_4$ (LFP)), and an electrolyte, mostly a lithium salt, such as $LiPF_6$, dissolved in an organic solvent. The charge and discharge processes in LIBs are described by the two half-reactions in Eqs. (1) and (2)

$$\text{Anode: } xLi^+ + xe^- + 6C \leftrightarrow Li_xC_6 \quad (1)$$

$$\text{Cathode: } LiMO_2 \leftrightarrow Li_{1-x}MO_2 + xLi^+ + xe^- \quad (2)$$

During charging, Li^+ ions released from the lithium metal oxide cathode migrate via electrolyte to the negative terminal, where they are inserted/intercalated into the graphite-based anode. Whereas during the discharge process, the Li^+ ions are extracted from the anode and then migrate back to the cathode. Interestingly, the free electrons produced during the Li^+ ion formation, which are also responsible for the completion of the half-reactions and are driven through an external wire and not via the electrolytes, as shown in Fig. 4.

2.3.1 *Limitations of the anode*

The graphite-based LIBs are the most predominant among other commercial LIBs owing to their ability to maintain their charge capacity after several charge–discharge cycles, which is associated with their low volume expansion during lithium intercalation. However, the capacity of these LIBs is limited because of the graphite structure, which allows the intercalation of just one lithium atom per six carbon atoms, i.e., LiC_6, thus leading to a low theoretical specific capacity of 372 mAh·g^{-1}, which is not sufficient to meet the ever-increasing energy demands (Table 2). However, aside from the lithium intercalation storage of the graphite anodes, alloying and conversion reaction mechanisms have also been

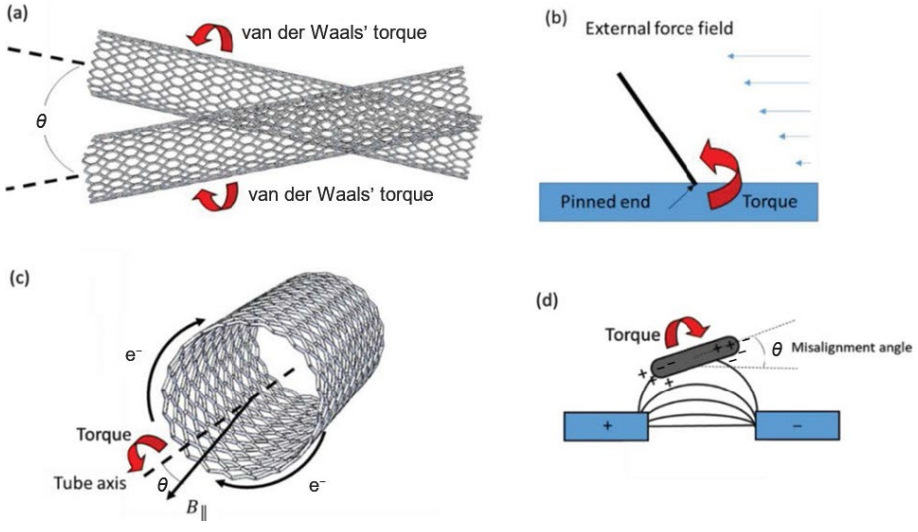

Figure 3 Different CNT alignment forces. (a) van der Waals' force. (b) Torque resulting from an external force. (c) Magnetic field force. (d) Dielectrophoresis-induced torque. Reproduced with permission from Ref. [116], © WILEY-VCH Verlag GmbH & Co. KGaA, Weinheim 2018.

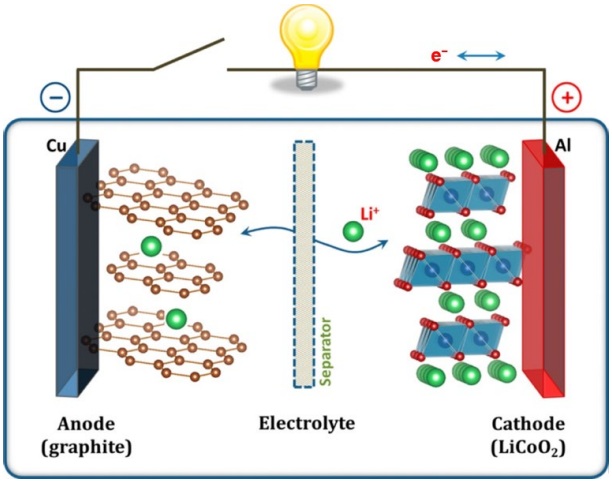

Figure 4 Schematic diagram of the LIB. Reproduced with permission from Ref. [129], © American Chemical Society 2013.

explored by researchers. Si and metals such as Al, Sn, and Sb store lithium by alloying with the lithium atoms to produce alloy-based anodes such as $Li_{4.4}Si$, LiAl, Al_4Li_9, $Li_{22}Sn_5$, and Li_3Sb with higher theoretical specific capacities of 4200, 993, 2234, 994, and 536 $mAh·g^{-1}$, respectively [126]. Despite their improved theoretical specific capacities, their usage as anode materials is hindered by pulverization which occurs because of the large volume change (expansion and contraction) during the alloying and dealloying processes, as seen in Table 1. This large volume change which occurs due to the bulk nature of the electrode materials compromises the metal-based anode's structural integrity, resulting in rapid capacity fading and severe safety issues [130].

The conversion reaction mechanism has also been touted to be a promising approach toward achieving a larger specific capacity because of its ability to utilize all possible oxidation states of the compound. Here, the conversion compound is converted to an entirely new product during lithiation alongside changes in structural and chemical properties. Several transition metal oxides, sulfides, nitrides, fluorides, and phosphides have been shown to successfully undergo conversion reactions [131–136], producing materials with improved electrochemical properties. However, the reaction mechanism is still not fully understood [137]. Similar to the alloying mechanisms, its commercialization has also been hindered by problems with pulverization, poor kinetics, cycle life, and irreversibility [138]. Figure 5 below shows a pictorial view of the material pulverization and electrode failure discussed above.

However, in order to overcome these issues of limited capacity and pulverization, there is the need to design nanostructured or nanostructured composite anodes with particle sizes in the nanometer scale [139]. Several designs have been proposed with varying degrees of success. Some of these approaches include the use of nanowires [12, 141–149], nanotubes [49, 143, 150–156], nanofibers [157–160], graphene flakes [161–165], hollow spheres [166–168], core–shell [169–173], composites [43, 174–177], and three-dimensional (3D) frameworks [178–182]. Among these materials, CNTs, especially the vertically aligned ones, have received great attention in recent years owing to their exceptional properties and their unique ability to be incorporated into other materials to form composites.

2.3.2 *Limitations of the cathode*

The cathode materials used in conventional LIBs have also drawn much attention in recent years. As mentioned earlier, the most widely used active cathode materials in LIBs are mainly inorganic salts such as $LiCoO_2$, $LiMn_2O_4$, and $LiFePO_4$. However, the use of these materials is fraught with different drawbacks. For instance, although $LiCoO_2$ has good cyclability and high theoretical specific capacity (274 $mAh·g^{-1}$) [183], its actual specific capacity is often restricted to 120–140 $mAh·g^{-1}$ [184, 185]. More so, its toxicity and high cost have also raised huge concerns about battery safety and price. $LiMn_2O_4$, on the other hand, is characterized by high operating voltage of up to 4.0–4.2 V vs. Li/Li^+ [186]. Compared to $LiFePO_4$, $LiMn_2O_4$ exhibits superior electrical and ionic conductivities [187]. However, the primary issues with the $LiMn_2O_4$ lie in its low theoretical specific capacity (148 $mAh·g^{-1}$) and fast capacity fading at high temperatures caused by Mn breakdown [188, 189]. Meanwhile, $LiFePO_4$ possesses a higher theoretical specific capacity (170 $mAh·g^{-1}$) and a much flatter charge/discharge potential curve at 3.45 V vs. Li/Li^+ than $LiMn_2O_4$, but suffers from poor rate capability due to its low electrical conductivity [190–192].

Lithiated transition metal phosphates have also been touted as promising cathode materials for LIBs. The most promising among them, lithium vanadium phosphate ($Li_3V_2(PO_4)_3$), has a high operating potential (3.0–4.8 V) and high theoretical specific capacity (197 $mAh·g^{-1}$) [193]. However, similar to $LiFePO_4$, its use has been hindered by the issue of poor electrical conductivity [186]. Vanadium pentoxide (V_2O_5) has also garnered much interest due to its high theoretical capacity of 440 $mAh·g^{-1}$ [194]. The high-capacity stems from its ability to theoretically hold up to three moles of lithium per mole of V_2O_5. Meanwhile, like the other cathode materials mentioned earlier, the V_2O_5 also suffers limited electrochemical performance due to poor electrical conductivity, low ion diffusion, and irreversible structural change emanating from multiple phase transitions during the charge–discharge process [195–197].

In the conventional LIBs, the conductivities of these active cathode materials are enhanced by coating the current collectors with slurries containing a mixture of the electroactive materials, conductive agents (such as carbon black), and polymer binders (for holding the electroactive materials and conductive agents together). Such cathode configurations are prone to huge internal electrical resistances resulting from the formation of different interfaces between the grain boundaries of the electroactive materials, conductive agents, and the current collectors [198]. These additional interfaces lead to increased charge transfer resistances and rapid capacity fading at high current rates [199].

However, this issue of poor electronic conductivity can be solved by integrating VACNTs as conductive networks into the LIB cathodes [200]. This facilitates electron and Li^+ ion transport, resulting in improved rate capabilities. The VACNTs also offer a significant improvement in energy density by allowing the deposition of more electroactive materials [201].

Table 2 Electrochemical properties of graphite and various group-IVA metals [140]

Anode material	Li intercalation stoichiometry	Theoretical specific capacity ($mAh·g^{-1}$)	Volume fluctuations (%)
C	LiC_6	372	< 5
Sn	$Li_{4.25}Sn$	959	257
Ge	$Li_{4.25}Ge$	1600	270
Si	$Li_{4.4}Si$	4200	300

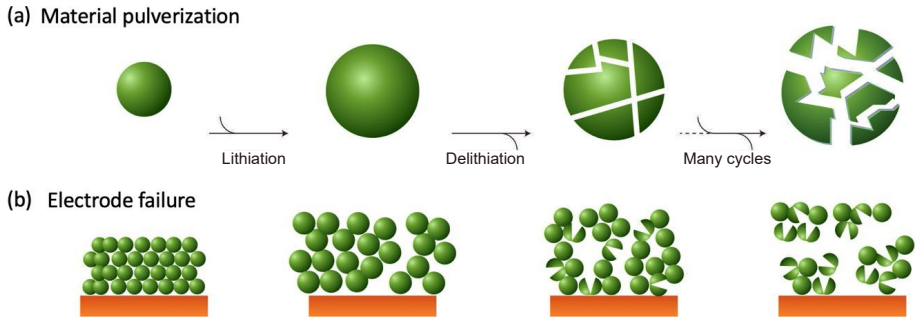

Figure 5 Schematic diagrams of the mechanical degradation of an electrode material at (a) the particle level and (b) electrode level during cycling. Reproduced with permission from Ref. [139], © Macmillan Publishers Limited 2016.

2.4 Mechanism of Li^+ storage in CNTs

As mentioned earlier, Li^+ ions are stored via three mechanisms: intercalation, alloying, and conversion reaction. Intercalation is common among the allotropes of carbon (graphene and CNTs), titanium disulphide (TiS_2), titanium dioxide (TiO_2), etc., while alloying and conversion reactions are employed by metals, metal oxides, phosphides, sulfides, fluorides, etc. As previously explained in this review, the alloy and conversion materials are susceptible to pulverization and electrode failure due to the large volumetric change (expansion and contraction) that occurs during lithiation and delithiation [130]. Thus, this discussion would be limited to the intercalation mechanism associated with CNTs.

Interestingly, the interior and exterior walls of CNTs are both electrochemically active locations for Li^+ ions intercalation. Thus, many studies, including theoretical works, have been done to succinctly probe the lithium storage mechanism employed by these materials [202–214]. In 2000, Yang et al. [202] examined the correlation between structure and charge–discharge behaviors of closed-end raw CNTs synthesized by the arc discharge method. They reported the difficulty in intercalating Li^+ ions inside the hollows of the tubes because of the closed ends. Thus, they proposed a mechanism in which the Li^+ ions can be intercalated or stored on the naked surfaces of the CNTs. Zhao et al. [203] also studied the Li^+ ions intercalation in CNT ropes using the first-principles method. They observed that both the interior and exterior interstitial spaces are favorable sites for lithium intercalation. Their result also showed a higher lithium density of LiC_2, which is significantly higher than the lithium density of LiC_6 seen in graphite. To determine which site is most favorable for lithium adsorption between the interior and exterior walls of CNTs, Senami et al. [207] applied *ab initio* quantum chemical calculations to investigate the adsorption of lithium atoms on the surface of the (12, 0) zigzag SWCNT. The result of their study showed that the inside wall of the SWCNT favors the adsorption of lithium atoms compared to the outside wall.

Furthermore, the Li^+ ion intercalation density is also influenced by the morphology of the CNT under consideration. Several studies have shown that defects affect the morphologies of CNTs, which invariably influence their capacities [204, 206, 208, 214–218]. For instance, Nishidate et al. [204] applied molecular dynamic calculations to investigate the diffusion behaviors of the Li^+ ions traveling into the SWCNT via the defects on the sidewall. Their results show that large defective sites favor the adsorption of Li^+ ions inside the SWCNT. The defects are formed by the removal of carbon atoms from the hexagonal carbon ring, leading to the occurrence of a hole in the CNT wall. The hole grows bigger as more carbon atoms are removed from the hexagon. The results from the molecular dynamic calculations by Nishidate et al. [204] reveal that although Li^+ ions can diffuse easily through the $n = 9$ defective ring, they are unable to diffuse through the defect-free ring, and $n = 7$ and $n = 8$ defective SWCNT rings.

It is also important to mention that, aside from the sidewalls of the CNTs, Li^+ ions can also enter the CNTs via the ends of open-ended CNTs. The result of the *ab initio* investigation of Li^+ ions diffusion in CNTs by Meunier et al. [212] reveals that Li^+ ions can enter through the $n = 9$ defective site or via the ends of open-ended CNTs. Their result also shows that the rate of diffusion of the ions is unrestricted once they enter inside the CNTs, provided that the tubes are short. Shimoda et al. [208] also reported an increased lithium storage capacity from LiC_6 in closed-end CNTs to LiC_3 after chemically etching the CNTs with a solution of H_2SO_4 and HNO_3 in a ratio of 3:1. They attributed the improved capacity to the Li^+ ions diffusion into the CNTs via the open ends and the sidewall defects introduced by the etching process. Thus, open-ended CNTs with shorter lengths are required to achieve high Li^+ ions diffusion rates inside the CNTs. The CNT length is essential in determining the diffusion coefficient, and this is because the Li^+ ions inserted into the tubes undergo a 1D random walk inside and are unable to leave if the tubes are too long, thus resulting in decreased effective diffusion rate. This explains the reason for the irreversible capacity that occurs in CNT anodes because some lithium-ions intercalated into the anode during the first cycle never make it back to the cathode.

3 VACNT-based anodes for LIBs

Ideal anode material for advanced LIBs should display higher capacity and improved charge–discharge rates than graphite [219]. In this regard, CNTs have been reported to display better lithium storage capacity compared to graphite due to their unique 1D structures and properties, enhanced conductivities as high as 10^6 and 10^5 $S \cdot m^{-1}$ for SWCNTs and MWCNTs, respectively, high tensile strength of up to 60 GPa, large specific surface area, mesoporous structure, low density, and high rigidity with Young's modulus of the order of 1 TPa [220–222]. SWCNTs have been reported to deliver reversible capacities of up to 700 $mAh \cdot g^{-1}$ [219, 223], a value almost twice the theoretical capacity of the graphitic anode.

The increased specific capacity and rate capability seen in CNT-based anodes are the consequence of the large surface area, reduced Li^+ ions diffusion, and electronic transport pathways offered by CNTs, properties that are peculiar to the nanoscale materials [30, 31]. In metal composite electrodes, the high mechanical strength and nanoscale size of the CNTs provide a solution to the bulk crystalline expansion and pulverization discussed earlier in this review. Herein, CNTs can act as support matrixes and flexible wire mesh to withstand the effect of the volume change and transport electrons to and from the active materials [224, 225].

3.1 Pristine VACNTs as anode materials for LIBs

Several studies [33, 201, 226–234] have suggested that VACNTs offer better electrochemical performance than graphite and their

randomly oriented counterparts. The improved performance results from a combination of the unique properties of VACNTs which are enumerated below.

- VACNTs possess larger surface area for better accessibility of electrolytes to electrodes and increased lithium storage.
- The highly aligned individual CNTs within the VACNT array are well attached to the current collector, ensuring fast charge transport by the formation of adequate 1D electron pathways.
- VACNTs possess 3D hierarchical structures for increased lithium storage and support for the deposition of electrochemically active materials.
- The regular inter-tube spacing and large pores facilitate the diffusion and accessibility of electrolytes.

Benefiting from their alignment in the vertical direction, VACNTs can create well-defined vertical channels in the direction of ion diffusion with reduced tortuosity, resulting in higher electronic conductivity and ionic diffusivity [49]. Thus, ions and electrons can easily be transported through the 1D channels to the surface of the active material and the current collector, respectively.

Chen et al. [226] studied the electrochemical performance of VACNTs fabricated on the surface of carbon nanofibers (CNFs) with active Ni bound on the other end of the CNTs. The anode delivered exceptional cyclic stabilities of 480.82 mAh·g^{-1} after 100 cycles at 100 mA·g^{-1} and 260.88 mAh·g^{-1} after 1000 cycles at a higher current density of 1000 mA·g^{-1}. It also displayed an impressive rate capacity of 262.06 mAh·g^{-1} at 1000 mA·g^{-1}. They suggested that the improved electrochemical performance shown by the anode was due to the multiple transport routes provided by the intimate connection between the aligned CNTs and the CNFs. They also recognized the impact of the gaps between individual CNTs and the large surface area for improved Li^+ ions diffusivity. Meanwhile, the randomly aligned MWCNTs synthesized by Frackowiak et al. [235] via catalytic decomposition of acetylene showed a high lithium storage capacity of 952 mAh·g^{-1} during the first cycle, which dropped significantly to 273 mAh·g^{-1} after five cycles. They attributed this to huge hysteresis loss typical for randomly oriented CNTs (RO-CNTs). Wang et al. [236] also obtained a reversible lithium storage capacity of 340–350 mAh·g^{-1} at low current density for randomly oriented MWCNTs prepared by the catalytic vapor deposition technique. Their result is similar to the reversible capacity of some graphite anodes.

In another study, Bulusheva et al. [229] examined the cyclic performance of VA-MWCNTs and disordered (DO)-MWCNTs electrodes, synthesized using 0.5% ferrocene. They reported specific capacities of 350 and 197 mAh·g^{-1} for the VA-MWCNTs and DO-MWCNTs, respectively, after 50 cycles. They attributed the higher specific capacity observed in the VA-MWCNTs to their larger surface area. Wang et al. [231] reported a high reversible capacity for VA-MWCNTs synthesized on a planar quartz substrate with nanocrystalline Fe as the catalyst. The VA-MWCNTs displayed a stable reversible capacity of 950 mAh·g^{-1} after the first cycle. Monalisa et al. [233] fabricated VA-MWCNTs with tree-like carbon nanostructures. The material also displayed a stable reversible capacity of 459 mAh·g^{-1} after 50 cycles. Masarapu et al. [230] reported an unusual but welcoming increase in the specific capacity with an increase in cycle number. They observed a 250% increase from 132 mAh·g^{-1} in the first cycle to 460 mAh·g^{-1} after 1200 cycles. They suggested that the anomalous behavior of the VA-MWCNTs could result from the structural alterations that took place with repeated cycling.

Welna et al. [33] also conducted a detailed study comparing the electrochemical performance of aligned and non-aligned CNTs. The VA-MWCNTs (Fig. 6(a)) were synthesized via pyrolysis of iron(II) phthalocyanine (FePc) on a quartz substrate under an Ar/H_2 environment. The alignments of the VA-MWCNTs were retained by Ni film support at the base, which also served as a current collector, as shown in Fig. 6(b). The non-aligned CNTs shown in Figs. 6(c) and 6(d) were also synthesized via the same technique, except that they were treated with hydrofluoric acid (HF) to detach the quartz substrate.

Upon electrochemical testing, as shown in Fig. 7(a), after the first cycle, the reversible capacity of the VA-MWCNTs decreased from 980 mAh·g^{-1} to a minimum near the 10th cycle but increased slightly afterward and stabilized near 750 mAh·g^{-1}. On the other hand, the reversible capacity of the non-aligned MWCNTs decreased steadily from 158 to 58 mAh·g^{-1} by the 34th cycle. Figures 7(b) and 7(c) are the voltage profiles of the different cycles

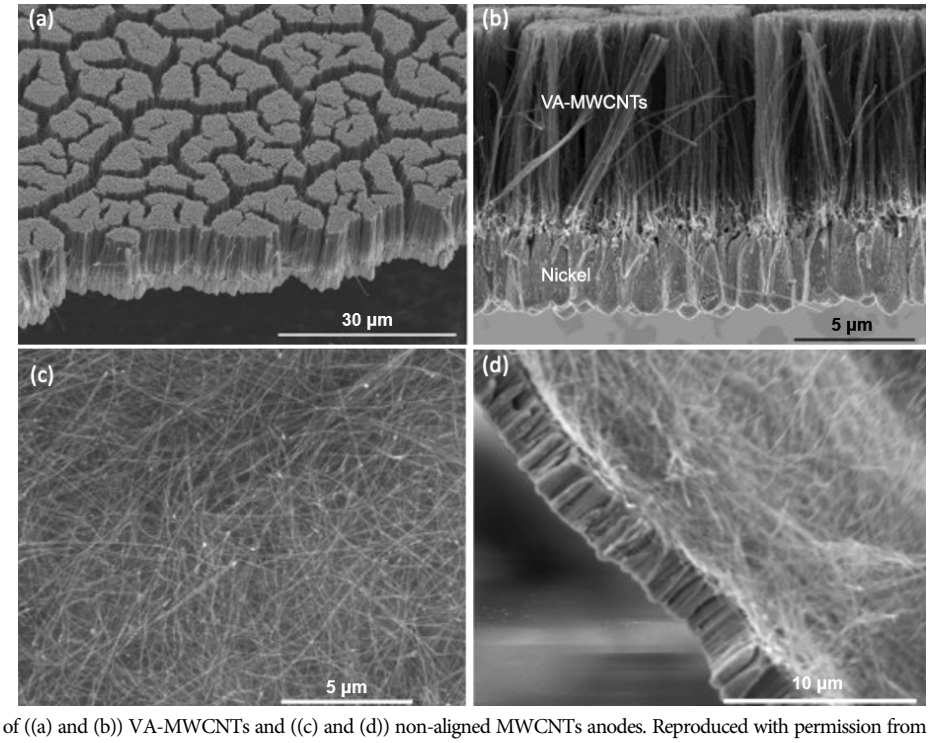

Figure 6 SEM images of ((a) and (b)) VA-MWCNTs and ((c) and (d)) non-aligned MWCNTs anodes. Reproduced with permission from Ref. [33], © Elsevier B.V. 2011.

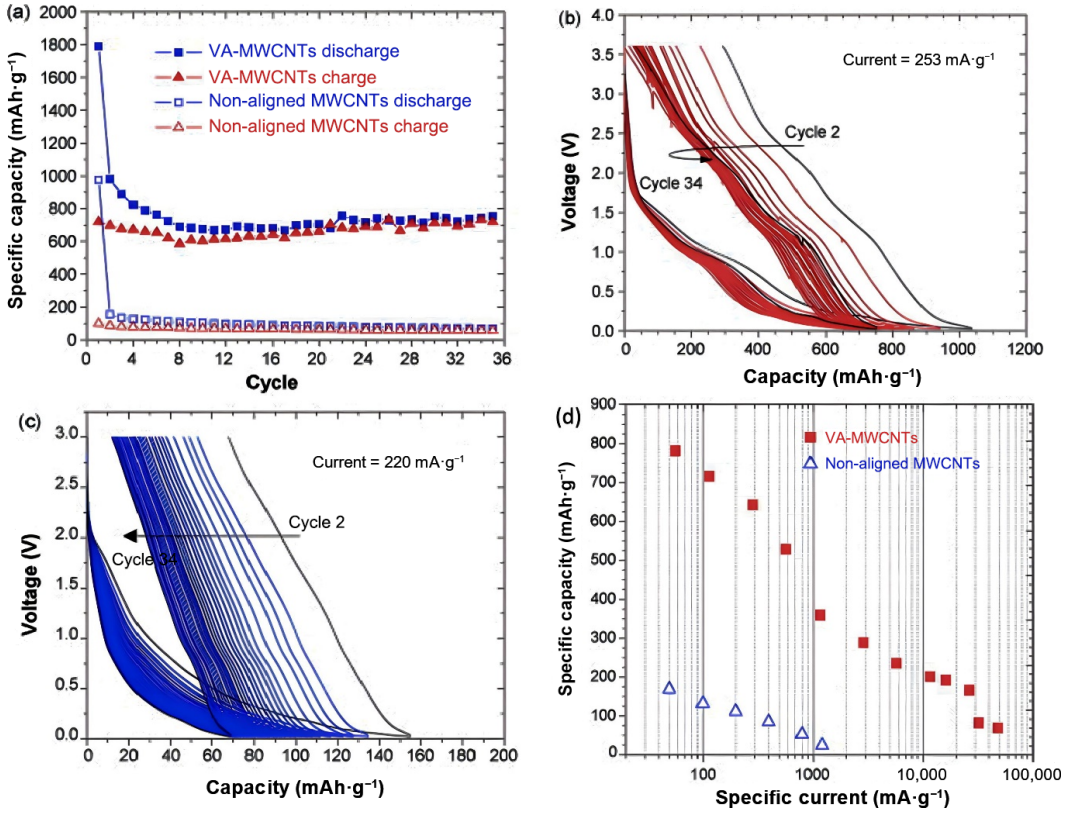

Figure 7 (a) Specific capacity as a function of the number of cycles for VA-MWCNTs and non-aligned MWCNTs at similar discharge rates. (b) Voltage profiles of cycles 2–34 for VA-MWCNTs and (c) voltage profiles for cycles 2–34 for non-aligned MWCNTs. (d) Specific capacity as a function of specific current for VA-MWCNTs and non-aligned MWCNTs electrodes. Reproduced with permission from Ref. [33], © Elsevier B.V. 2011.

reported in Fig. 7(a). They concluded that the significantly improved reversible capacity observed for the VA-MWCNTs was due to the alignment of the nanotubes in the direction of ion diffusion, which allows for more Li^+ access to the nanotubes.

The rate capabilities of both the aligned and non-aligned CNTs were also studied (Fig. 7(d)). The maximum reversible capacity of 782 mAh·g^{-1} was observed for the VA-MWCNTs at a current density of 57 mA·g^{-1}. This result is obviously more than twice the theoretical capacity of the graphite anode (372 mAh·g^{-1}). However, the capacity decreased with an increase in the current density because of the reduced ion diffusion at high current densities [127]. Nonetheless, the reversible capacity never went below 166 mAh·g^{-1} until the current density exceeded 26 A·g^{-1}. On the contrary, the non-aligned MWCNTs displayed lower rate capabilities than the VA-MWCNTs. The maximum value was 169 mAh·g^{-1} at 50 mA·g^{-1}, which decreased to 26 mAh·g^{-1} at 1200 mA·g^{-1}. Again, they concluded that the improved rate capability of the VA-MWCNT electrode resulted from the alignment of the individual CNTs. The orderly alignment of VA-MWCNTs ensured intimate contact between each individual CNTs and the Ni current collector. This enabled each of the VA-MWCNTs to partake in the cycling of the electrode, thereby maintaining electrical continuity. In contrast, due to their disorderliness, the non-aligned MWCNTs suffer from huge hysteresis loss. The nanotubes are not directly attached to the current collector but rely on the contact between each other for electrical continuity.

Lu et al. [201] addressed the multiple challenges faced by the state-of-the-art LIBs (energy density, power density, safety, and lifespan) by using a VACNT anode synthesized directly on Ni foil substrate. The anode delivered a high reversible capacity, and high energy and power densities of 600 mAh·g^{-1}, 297 Wh·kg^{-1}, and 12 kW·kg^{-1}, respectively, at 0.25 C. As expected, they attributed this improved performance to the unique porous structure, larger surface area of the VACNTs, and the intimate contact between individual CNTs and the Ni current collector. Kathleen et al. [156] also demonstrated high electrochemical performance for the VA-SWCNT LIB anode. The VA-SWCNTs were synthesized directly on Inconel foils and later assembled in a half-cell configuration for performance testing. After 300 cycles at 1 C (1 C = 372 mA·g^{-1}), the VA-SWCNT anode still delivered exceptionally high charge and discharge capacities (both > 1200 mAh·g^{-1}). The post-mortem imaging study also revealed that the SWNCTs maintained their vertical alignment across the Inconel substrate. This again confirms the effect of the high conductivity, large surface area, and exceptional mechanical strength possessed by VACNTs.

Abdollahi et al. [32] also reported high electrochemical performance for a 3D flexible anode fabricated by synthesizing VACNTs on porous a-rGO paper using a plasma-enhanced chemical vapor deposition (PECVD) technique. The VACNTs served as an electrical conduction route to enhance Li^+ ion intercalation. The result of the electrochemical performance revealed a large initial discharge capacity of 1401 mAh·g^{-1} and a high reversible capacity of 459 mAh·g^{-1} at 150 mA·g^{-1}. After 100 cycles, the anode displayed a stable capacity of 459 mAh·g^{-1}, which is more than the theoretical specific capacity for graphite. As expected, they attributed this improved performance to efficient conducting paths offered by the VACNTs as well as their role in improving the accessible surface area. Table 3 below compares the electrochemical performances of vertically aligned and randomly oriented CNT anodes as reported in other literatures not previously discussed.

Although the pristine VACNTs offer considerable improvement to the specific capacity compared to the graphitic anode, their full potential as stand-alone anode materials is yet to be actualized owing to a number of issues. Firstly, due to the large active surface area and the presence of defects on the surface of the CNTs, during the initial charging process, an increased amount of

Table 3 Electrochemical performances of VACNTs and RO-CNTs from different studies[a]

Material	C_{re} (mAh·g^{-1})	C_{irre} (mAh·g^{-1})	Current density (mA·g^{-1})	Number of cycles	References
RO-SWCNTs	460	1200	20	—	[237]
RO-MWCNTs	250	250	50	—	[238]
RO-SWCNTs	600	1400	50	—	[238]
VACNTs/G	897.83	—	100	5	[239]
VACNTs/G	525	2350	500	1000	[240]
VACNTs	557	2350	2 C	20	[232]

[a] C_{irre} is the reported first cycle irreversible discharge capacity while C_{re} is the reversible discharge capacity after N number of cycles.

Li^+ ions partake in the formation of the so-called solid electrolyte interface (SEI) and are not recovered from the electrolyte upon discharge [219, 241]. This leads to colossal irreversible capacity loss, thus, poor initial CE. For a more detailed understanding of how the SEI is formed, the following review articles are highly recommended [242–245]. Secondly, the CNTs undergo broad voltage changes during discharge, limiting their use in portable electronic devices that require a stable voltage supply. These drawbacks are most likened to the difficulty in obtaining consistent structures and morphologies during synthesis. Thus, there is a need to fabricate novel nanostructured materials that could combine the unique properties of the VACNT and the compositing material.

3.2 VACNT composite anodes

VACNTs can be integrated as a support matrix to other electrochemically active materials like Si, Ge, metal, and metal oxide nanoparticles to form composite electrodes with highly improved battery performance. The resulting CNT-metal composite anode systems employ two mechanisms for lithium storage: the alloying or conversion and intercalation mechanisms of the electroactive materials and CNTs, respectively. These composite systems take advantage of the electroactive materials' high lithium storage capacity without compromising the materials' structural integrity during the lithiation and delithiation processes. During charging, the electroactive materials alloy themselves with Li^+ ions, leading to an increase in size. Still, the structure is maintained because the CNTs are there to act as a flexible wire mesh, allowing the electroactive materials to remain attached to the current collector. It has also been demonstrated by researchers that CNTs improve the stability of the SEI layers formed during initial cycling in composite electrodes. The CNTs limit the volume change of the anode and ensure that the SEI layers are firmly attached to the active materials' surface during subsequent cycling [246–248]. More so, aside from the CNTs acting as a glue matrix to the active materials, they also store any extra Li^+ ions that are not alloyed with the active materials, leading to highly improved storage capacity. The huge irreversible capacity loss issue is also minimized in the composite structures. In fact, a group [249] argued that proper deposition of active materials onto the surfaces of CNTs reduces the specific surface areas of CNTs exposed to Li^+ in the electrolyte, leading to significantly reduced first-cycle irreversible capacity loss (improved initial CE).

However, compared to the randomly oriented CNTs, VACNTs are best suited for the formation of these composite electrodes. As mentioned earlier, this results from their inherent well-defined pore structure, perfectly aligned 1D conductive electron pathways, larger surface area, and regular inter-tube spacing that can accommodate the internal stress induced by lithium-ion insertion and extraction.

3.2.1 Silicon-VACNT composites

Si, which is the second most abundant element on earth, is viewed as the most promising choice for anode materials in LIBs because of its remarkably high lithium storage capacity (~ 4200 mAh·g^{-1} for $Li_{4.4}Si$) and the high melting point of its lithium compounds. It also has a higher operating potential than lithium, inhibiting metallic-lithium deposition in the case of overcharge. However, using pristine Si as an anode material is fraught with some issues. Firstly, the Si anode suffers low CE as a result of pulverization [250]. Like metals, Si undergoes large volumetric changes during alloying and dealloying (charge and discharge). The SEI formed during the first lithiation process is repeatedly destroyed due to this volume change. Meanwhile, new SEI films are continually formed on the Si surfaces exposed by pulverization. This phenomenon leads to huge irreversible loss owing to the consumption of a massive amount of Li^+ ions during repeated SEI film formation. More so, when pulverization occurs, the anode loses contact with the current collector, resulting in anode failure after just a few cycles. Secondly, during alloying and dealloying, the crystalline Si nanoparticles become partially amorphous, which is known to have lower conductivity than the crystalline ones. This structural alteration to the less conductive amorphous Si makes it difficult for the current to reach the current collector. Thirdly, overall electronic transport within pristine Si anodes is poor due to the inherent semiconducting nature of elemental Si.

However, using CNTs as conductive networks and support frameworks is essential in facilitating electronic movement, preventing electrode crumbling (improving CE), and enhancing SEI stability. Thus, there have been several studies on this effect [234, 251–260].

In a bid to explore the effect of CNTs on the electrochemical performance of Si-based anodes, Xue et al. [251] studied the performances of pure Si, carbon-coated Si nanoparticles (Si@C), and carbon-coated Si nanoparticles dispersed in randomly aligned CNT networks (Si@C-CNTs). The pure Si electrode delivered initial charge and discharge capacities of 4299 and 2780 mAh·g^{-1}, respectively, correlating with a low initial CE of 65%. The low CE was attributed to large irreversible capacity loss caused by the colossal volume changes and loss of electrical connections between Si nanoparticles. Poor cycling performance was also reported as the first cycle reversible capacity of 2780 mAh·g^{-1} decreased drastically to 100 mAh·g^{-1} after 40 cycles. The Si@C, on the other hand, offered improved electric conductivity and cushioned the large volume change of the active Si, giving room for 75% CE, 48% capacity retention, and reversible capacity over 100 mAh·g^{-1} after 40 cycles. However, although the Si@C-CNTs offered the least reversible capacity and CE of 699 mAh·g^{-1} and 54% among the three electrodes, they demonstrated the best cycling stability and the highest capacity retention of up to 70% after 40 cycles. The low CE was reported to be as a result of poor CE of randomly aligned CNTs.

Meanwhile, higher CE, reversible, and retention capacities have been achieved with VACNTs/Si composites, as shown in Table 4. For instance, Fu et al. [253] studied the electrochemical

Table 4 Electrochemical performances of some selected VACNTs/Si composite studies

Anode system	Reversible capacity ($mAh·g^{-1}$)	Capacity retention (%)	Coulombic efficiency (%)	Current density ($mA·g^{-1}$)	Number of cycles	References
VACNTs/Si	1100	51	99.5	0.2 C	100	[261]
VACNTs/Si	765	—	98	15 C	100	[262]
VACNTs/Si core–shell	2502	90.4	—	420	100	[257]
VACNTs/Si core–shell	2510	91	99	420	80	[259]
3D VACNTs/Si	2562	93	—	1000	100	[252]
3D VACNTs/Si	1687	94.4	99.7	—	200	[234]
Patterned VACNTs/Si	650	—	~ 95	400	10	[263]

performance of a free-standing, binder-free, and flexibly aligned CNT-Si sheet anode coated with an additional layer of carbon. The aligned CNT sheet was used as the current collector and the electrochemically active substrate on which the Si was deposited. In addition, the aligned nature of the CNTs enabled the uniform deposition of Si by providing significant inter-tube spacing. This novel nanostructure delivered initial charge and discharge capacities of 1801 and 2270 $mAh·g^{-1}$, respectively, corresponding to an initial CE of 79%. Upon further cycling at a high current density of 100 $mA·g^{-1}$, an excellent reversible capacity of 1494 $mAh·g^{-1}$, CE of ~ 98%, and capacity retention of more than 94% after 45 cycles were obtained. In the same experiment, they also examined the rate capability of this material by measuring the specific capacity at different current densities (50, 100, 200, 400, and 800 $mA·g^{-1}$). They obtained high capacities of around 1720, 1600, 1500, 1250, and 1000 $mAh·g^{-1}$ for the respective current densities.

Yildiz et al. [254] also examined the electrochemical performance of a similar composite anode system prepared by electrospinning polymethyl methacrylate (PMMA)-Si nanofibers onto aligned CNT sheets. The structure was coated with pyrolytic carbon to hold the Si nanoparticles firmly within the CNT sheets and stabilize the formation of SEI, which could lead to a huge irreversible loss. A high reversible capacity of 1470 $mAh·g^{-1}$, improved retention capacity of 88%, and high CE of 98% after 150 cycles at a high current density of 100 $mA·g^{-1}$ were reported. In 2015, Epur et al. [258] studied the electrochemical performance of a simple binder-free scribable electrode comprising vertically aligned Si-coated MWCNTs (VASCNTs) on a copper foil. The scribed electrode displayed a high discharge capacity of over 3000 $mAh·g^{-1}$ and a low irreversible loss of 19% during the first cycle. The electrode also showed improved cycling performance with high retention capacity and CE of 76% and 98.5%, respectively.

Wang et al. [38] were the first to report the lowest first-cycle irreversible loss of 6% for a nano-hierarchical Si anode. They fabricated the anode by synthesizing VACNT arrays directly on Inconel substrate and subsequently depositing Si on the as-synthesized VACNTs. Upon electrochemical testing, the resulting nanostructured VASCNT electrode delivered very high charge and discharge capacities of 1958 and 2078 $mAh·g^{-1}$, respectively, with an initial CE of 94%. This corresponds to an initial capacity loss of 6%. Subsequent cycles resulted in a much higher CE of 99.5% and a fairly constant capacity with a loss of ~ 0.3% per cycle. They attributed this performance to the combined effect of the unique properties of the VACNT arrays and the high lithium storage capacity of Si.

In an earlier study, Wang et al. [249] reported the synthesis of 1D heterostructures consisting of VACNTs coated with amorphous/nanocrystalline Si droplets via a facile two-step liquid injection CVD process. Figures 8(a) and 8(b) show the SEM images of the as-grown VACNTs and the hybrid VACNTs/Si nanostructures. It can be clearly seen from Fig. 8(b) that the

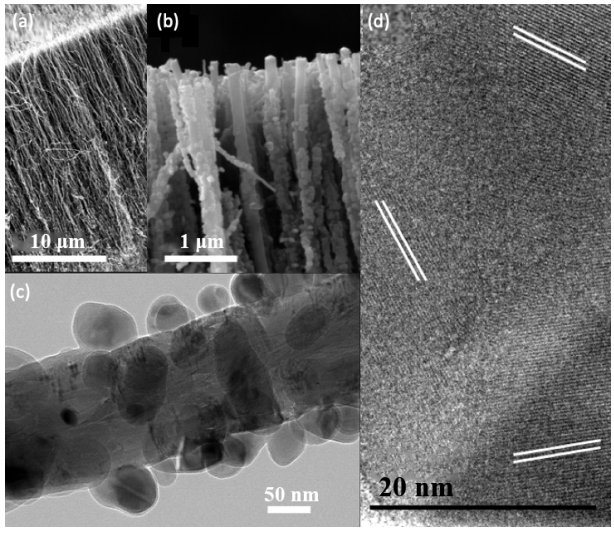

Figure 8 SEM images of (a) as-grown VACNTs and (b) VACNTs coated with Si nanoparticles. (c) TEM image of a single VACNT coated with multiple Si nanoparticles. (d) HR-TEM image of a single Si nanoparticle showing the crystal lattice orientations. Reproduced with permission from Ref. [249], © American Chemical Society 2010.

VACNTs retained their vertical alignment after Si deposition. Figure 8(c) is the transmission electron microscopy (TEM) image of a single Si-coated tube, while Fig. 8(d) is the high-resolution TEM (HR-TEM) image of the hybrid structure showing the crystal lattice orientations within an Si nanoparticle.

Upon electrochemical testing, the hybrid VACNTs/Si nanostructures anode delivered first discharge and charge capacities of 2552 and 2049 $mAh·g^{-1}$, respectively, as shown in Fig. 9(a). This corresponds to an irreversible capacity loss of 19.7% and initial CE of 80.3%. However, the CE reaches 99% in the subsequent cycles alongside slightly increased discharge and charge capacities due to the activation of more Si atoms. The hybrid structure also exhibited an excellent rate capability, delivering a high capacity of ~ 1000 $mAh·g^{-1}$ at 2.5 C, a value three times more than that of graphite (Fig. 9(b)).

Despite the enormous prospects of these materials, their commercialization and practical applications are still hampered by the high cost of elemental Si preparation methods.

3.2.2 *Germanium-VACNTs composites*

Ge has been reported to possess a high theoretical capacity of ~ 1600 $mAh·g^{-1}$, high electronic conductivity, and lithium diffusivity [264, 265]. However, Similar to pure Si anodes, pristine Ge anodes are also susceptible to pulverization which occurs as a result of large volumetric change during alloying and dealloying, leading to loss of electrical contact between the current collector and the active material (Ge) as shown in Fig. 10(a). This invariably causes a huge fractional loss of capacity during cycling [266, 267],

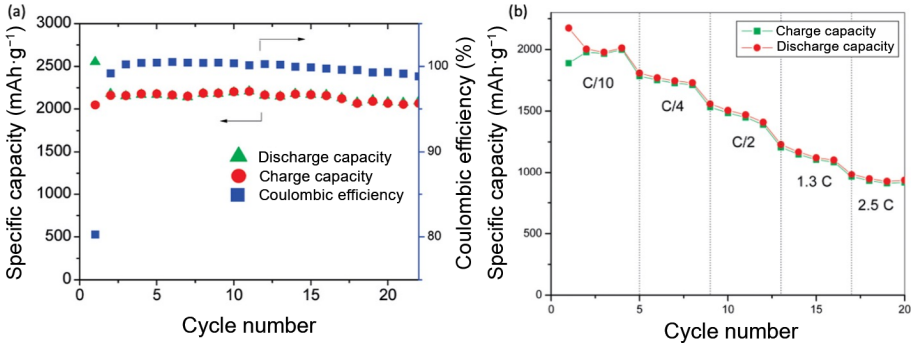

Figure 9 (a) Charge/discharge curves and CE of the hybrid VACNTs/Si anode over 25 cycles at 100 mA·g^{-1}. (b) Rate capability of the hybrid anode at different charge and discharge current rates. Reproduced with permission from Ref. [249], © American Chemical Society 2010.

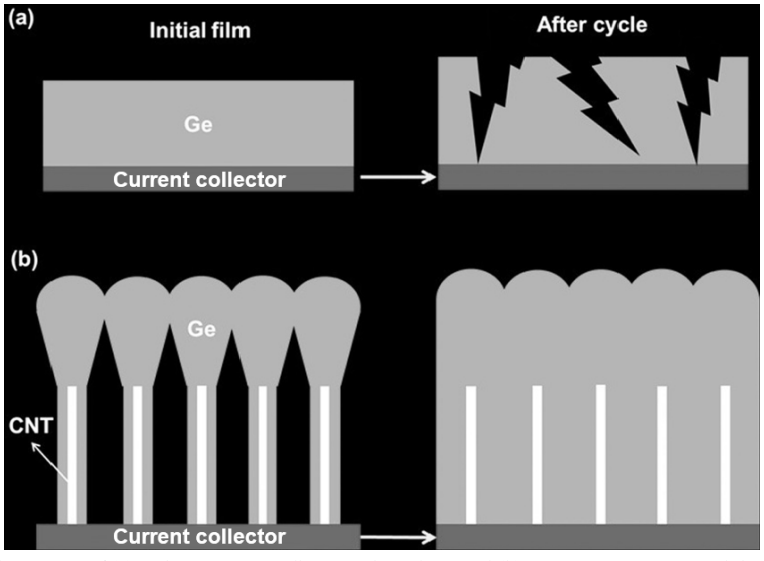

Figure 10 Schematic diagrams of structures of (a) a planar current collector with Ge layer and (b) a 3D VACNT supported thick Ge film before and after cycling. Reproduced with permission from Ref. [270], © Wiley-VCH Verlag GmbH & Co. KGaA, Weinheim 2014.

leading to low CE. The intrinsic semiconductive nature of elemental Ge also prevents efficient electron transport. To mitigate these issues, researchers have explored the combination of CNTs and Ge to form a composite, which has proven to be the best alternative.

In 2014, Susantyoko et al. [268] reported the performance of amorphous polycrystalline Ge on VA-MWCNT arrays (MWCNT/c-Ge) and amorphous Ge on the identical MWCNT arrays (MWCNT/a-Ge) as active materials for LIBs. Figures 11(a)–11(c) show the SEM images of the as-synthesized VA-MWCNTs, c-Ge coated VA-MWCNTs, and a-Ge coated VA-MWCNTs. According to Fig. 12(a), during the first cycle, the MWCNT/c-Ge displayed discharge and charge capacities of 955.6 and 710.8 mAh·g^{-1} at 0.1 C, with an initial CE of 71.3%. After the first cycle, the specific capacity became more stable from the second to the 100th cycle, decreasing from 774.3 to 730.2 mAh·g^{-1} with an improved CE of over 95%. Similarly, the MWCNT/a-Ge showed high first-cycle discharge and charge capacities of 1725.8 and 1234 mAh·g^{-1}, corresponding to an initial CE of 73.5%, at a current density of 0.1 C, as shown in Fig. 12(b). Interestingly, after 100 cycles, it still showed a very high specific capacity of 1096.1 mAh·g^{-1} with CE above 95%. Although they reported that the VA-MWCNTs contributed to less than 5% of the specific capacity of the entire structure, they attributed the cycling stability reported in both cases to the VA-MWCNT role as a support matrix to mitigate pulverization. Gao et al. [269] also reported excellent rate capability and highly improved stability for a graphene/CNT (GCNT) hybrid structure coated with Ge. The Ge/GCNTs anode displayed a specific capacity of over 800 mAh·g^{-1} at a very high current density of 40 A·g^{-1} after 200 cycles.

Wang et al. [270] used VACNT arrays as a 3D current collector to enhance the electrochemical performance of a 1020-nm-thick Ge film, as shown in Fig. 10(b). After 100 cycles, the VACNT-supported electrode structure exhibited a high reversible capacity of 1314 mAh·g^{-1} and an impressive capacity retention of 97.2% at a rate of 0.2 C (1 C = 1600 mA·g^{-1}). It also showed an impressive rate performance, with a high reversible capacity of more than 843 mAh·g^{-1} at a rate of 10 C. These improvements were attributed to the presence of more free spaces offered by the VACNTs to withstand the huge volume change and provide rapid electron transport.

All these studies strongly underlie the exceptional electrochemical performances of the Ge-VACNT composite electrodes and portray them as a promising and highly competitive alternative in LIB anodes. Nevertheless, their commercialization remains a critical issue yet to be addressed because of the high cost of production.

3.2.3 *Tin-VACNT composites*

Sn has also been considered a promising candidate to replace the graphitic anodes owing to its theoretical specific capacity of 992 mAh·g^{-1} (for its $Li_{22}Sn_5$ alloy) [271] and relatively huge abundance in nature. However, similar to Si and Ge, their usage is also hindered by large volumetric change upon lithiation and delithiation, which results in pulverization and poor cycling performance [272]. CNTs have been incorporated with Sn for composite anode systems to abate this issue.

Sun et al. [273] reported the electrochemical performance of a binder-free LIB anode based on an Sn-coated VACNT array synthesized on a stainless steel (SS) substrate. Figure 13(a) shows

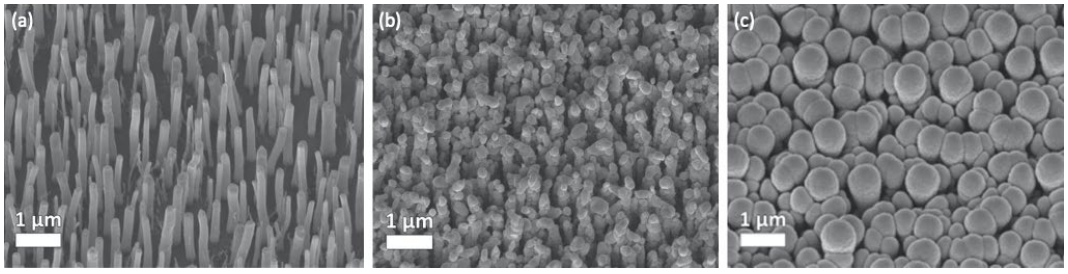

Figure 11 SEM images of (a) as-synthesized VA-MWCNTs, (b) c-Ge coated VA-MWCNTs, and (c) a-Ge coated VA-MWCNTs. Reproduced with permission from Ref. [268], © Elsevier Ltd. 2014.

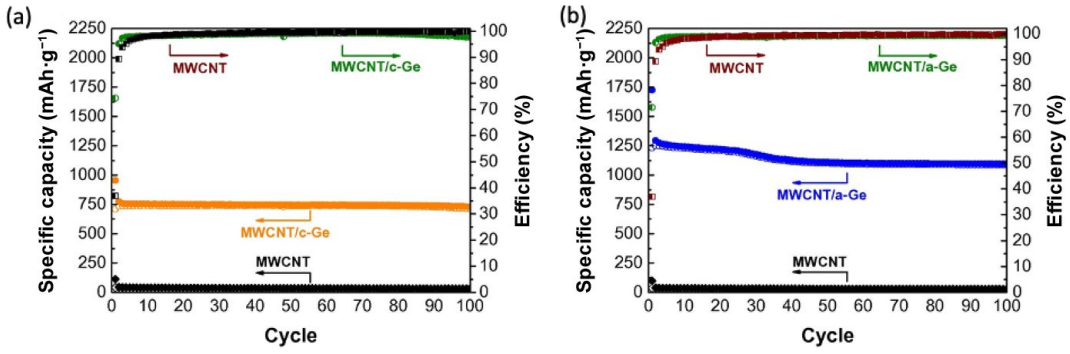

Figure 12 Cyclic performance of (a) MWCNT/c-Ge and (b) MWCNT/a-Ge at constant current rate of 0.1 C for 100 cycles. Reproduced with permission from Ref. [268], © Elsevier Ltd. 2014.

VACNTs synthesized on the SS current collector with an average diameter of 20 nm. Upon coating with Sn, the average diameter increased to 100 nm but still maintained large inter-tube spacing for efficient strain accommodation (Fig. 13(b)). The authors compared the Sn mass loading on the Sn-coated VACNTs and flat Sn film, and they observed that the Sn mass loading on the VACNT sample was larger than that of the flat Sn film by a factor of 1.3–1.4. This was obviously due to the improved surface area offered by the VACNTs, allowing for more active materials to be loaded on them.

As shown in Fig. 14(a), after 400 cycles, the Sn-VACNT composite anode delivered a reversible capacity of 930.8 mAh·g^{-1} at 0.2 C with an initial CE of ~ 80%. Prolonged cycling (1000 cycles) at 0.5 C also delivered a considerably high specific capacity and CE of 380.9 mAh·g^{-1} and 99.37%, respectively (Fig. 14(b)). The rate performance at current densities from 0.1 to 1.0 C was also evaluated. Figure 14(c) shows that the composite anode delivered excellent rate stability and specific capacities even after 200 cycles. Upon reversing the current density to the initial 0.1 C, the initial specific capacity of 953.5 mAh·g^{-1} was also restored.

Furthermore, to distinguish the impact of the VACNT structure, three different electrodes consisting of pure VACNT, flat Sn film, and Sn-coated VACNT anodes were fabricated for electrochemical testing. From Fig. 14(d), although the pure VACNT anode showed very low specific capacity when compared to the other two, it showed the least degradation (high stability) across the 100 cycles. When compared to the Sn-coated VACNT, the Sn film electrode showed very fast degradation and lower specific capacity resulting from pulverization. This improved stability and specific capacity seen in the Sn-coated VACNT electrode is a result of high mechanical strength, porous nature, and large surface area offered by the VACNTs in the composite.

Deng et al. [274] reported improved electrochemical performance for a 3D tin disulfide (SnS_2)/VACNTs anode. The anode exhibited an excellent specific capacity of 551 mAh·g^{-1}, a good cyclability of 551 mAh·g^{-1} at 100 mA·g^{-1}, and an impressive rate capability of 223 mAh·g^{-1} after 100 cycles. They attributed the high performance to the combined effect of SnS_2 and the presence of the nanostructured VACNT arrays. The VACNTs served both as conductive additives and support-framework to enhance the conductivity of SnS_2 and accommodate the effect of volume change during cycling.

3.2.4 *VACNT-metal oxide composites*

As stated earlier, CNTs can be incorporated into metal oxides to form composite materials for LIB anodes. These materials are touted to be the most promising candidates to replace conventional graphitic anodes. They can offer thrice the gravimetric capacity of graphite with minimal capacity fading over several cycles [130]. Similar to Si and Ge, which have been discussed earlier, pristine metal oxide anodes suffer from pulverization due to high volumetric changes that occur during charging and discharging. As we already know from our discussion so far, this phenomenon results in severe capacity fading and battery failure. To abate this issue, CNTs have been used as scaffolds or support matrices to withstand the volume changes of the metal oxides during cycling owing to their unique tensile strength, leading to improved cyclability. Such composite materials would utilize two lithium storage mechanisms: intercalation and alloying or conversion reactions, leading to an increased specific capacity. In addition to the enhanced cyclability and increased specific capacity, the CNT/metal oxide composites offer improved rate capability because the CNTs can also act as a conducting wire to improve electronic transport. Several groups have reviewed the performances of the CNT/metal oxide composite anodes but with little or no emphasis on the aligned CNTs, despite their excellent prospects in energy storage applications [275–283]. Thus, in this section of our review, we will restrict our discussions to only aligned CNT/metal oxide composites.

Owing to their unique properties discussed earlier, aligned CNTs have been integrated into different metal oxides to form composite anode for LIBs. In 2018, Zhu et al. [284] fabricated a free-standing and binder-free TiO_2/SACNT hybrid film that can be used as flexible anodes in LIBs. The SACNT arrays were synthesized on Si wafers in a low-pressure CVD system. The composite anodes were fabricated via the sol-gel technique by dispersing the SACNT arrays in a mixture of ethanol, ammonia-

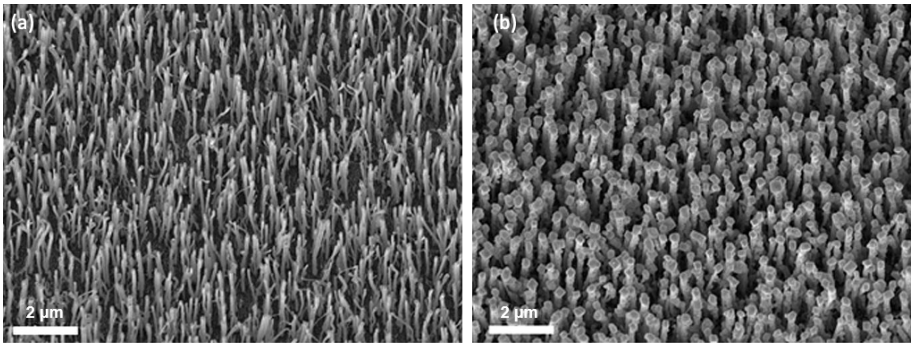

Figure 13 SEM images of (a) as-synthesized VACNT array and (b) Sn-coated VACNT array. Reproduced with permission from Ref. [273], © Elsevier Ltd. 2014.

water, and tetrabutyl titanate (TBT). Afterward, the electrochemical performance of the TiO_2/SACNT films was investigated in half cells, using pristine lithium foils as both counter and reference electrodes. After 1000 cycles, the TiO_2/SACNT films still delivered impressive capacities of 190, 145, 135, 125, 120, and 100 mAh·g^{-1} at high current densities of 1, 5, 10, 20, 30, and 60 C, respectively, with CE of nearly 100% at each cycle. They also reported that the structure of the TiO_2/SACNT composite was intact after 1000 cycles at 60 C. They attributed the excellent electrochemical performance to the flexibility of the SACNTs due to their nanoscale diameter (~ 10 nm), the highly conductive nature of the SACNTs for improved electron transport, and the large surface area offered by the SACNTs for a large amount of lithium storage.

Aside from the TiO_2, aligned CNTs have also been used to form composite anode systems with other titanium-based oxides, such as $Li_4Ti_5O_{12}$ (LTO), with impressive results [285–287]. LTO displays some impressive advantages over conventional graphite-based anodes, such as flat and relatively high redox potential (1.55 V vs. Li$^+$/Li) [288]. This results in a decreased cell potential of the LIB, obviating electrolyte decomposition and SEI formation. This enables the LTO electrodes to withstand high current densities [289]. Despite these excellent properties, the LTO is fraught with low electronic conductivity (< 10^{-13} S·cm^{-1}) [290] and a relatively low Li$^+$ ion diffusion coefficient [291], culminating in a low-rate performance. However, the electronic conductivity and Li$^+$ ion diffusivity can be enhanced by coating the LTO nanoparticles on highly conductive aligned CNTs. For instance, Pawlitzek et al. [285] fabricated a VACNT/LTO composite anode by decorating VACNTs synthesized on Ni foil with LTO nanoparticles via spray deposition technique. The open-pore nature of the VACNT arrays contributed immensely to the high effectiveness of the spray deposition technique. Samples with four different LTO loads were prepared (45 wt.%, 60 wt.%, 70 wt.%, and 78 wt.%), and their electrochemical performance was investigated in coin cells by cyclic voltammetry (CV). The specific capacity dropped from 185 mAh·g^{-1} in the low LTO load sample (45 wt.%) to 135 mAh·g^{-1} in the high LTO load sample (78 wt.%) at 2 C (1 C = 175 mAh·g^{-1}) (Fig. 15(a)). The higher performance observed in the low LTO sample was attributed to the relatively higher CNT content and the narrow size distribution of the LTO nanoparticles (~ 25 nm), offering a more specific surface area for Li$^+$ ions storage. Furthermore, the rate capability was tested at extremely high current densities (up to 500 C). As shown in Fig. 15(b), all the coin cells display high specific capacities at very low discharge rates below 2 C. However, the 78 wt.%, 70 wt.%, and 60

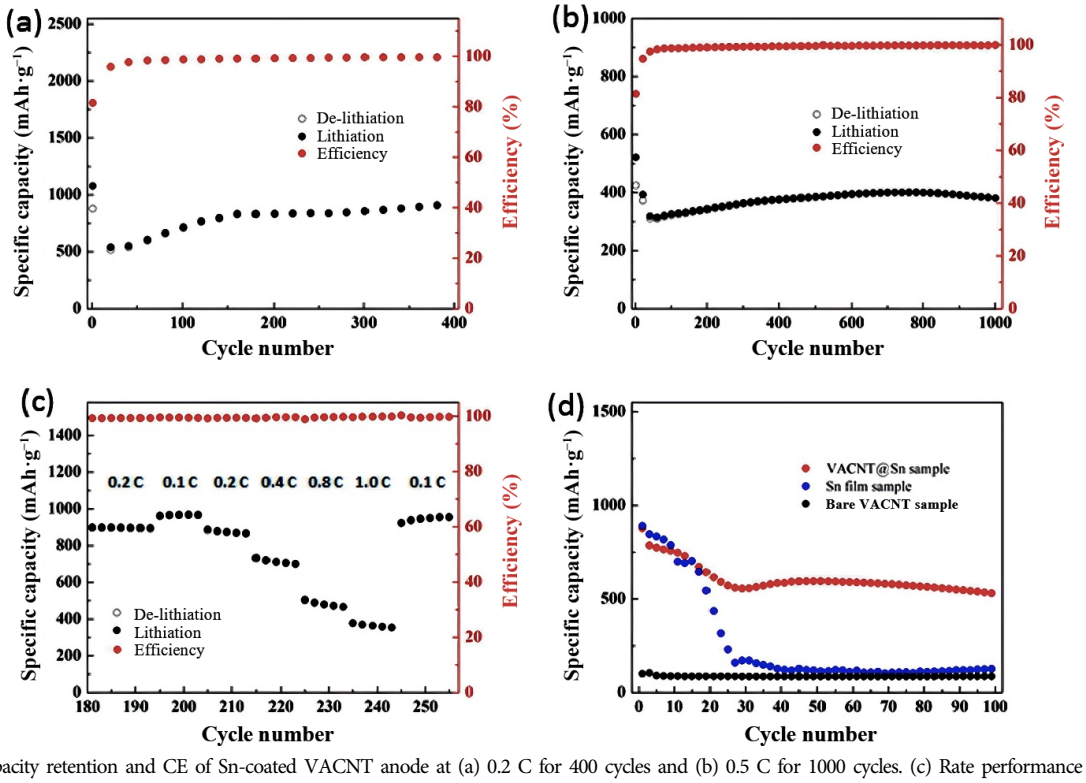

Figure 14 Capacity retention and CE of Sn-coated VACNT anode at (a) 0.2 C for 400 cycles and (b) 0.5 C for 1000 cycles. (c) Rate performance of Sn-coated VACNT anode from 0.2 to 1.0 C and back to 0.1 C. (d) Reversible capacities of pure VACNT, flat Sn film, and Sn-coated VACNT anodes. Reproduced with permission from Ref. [273], © Elsevier Ltd. 2014.

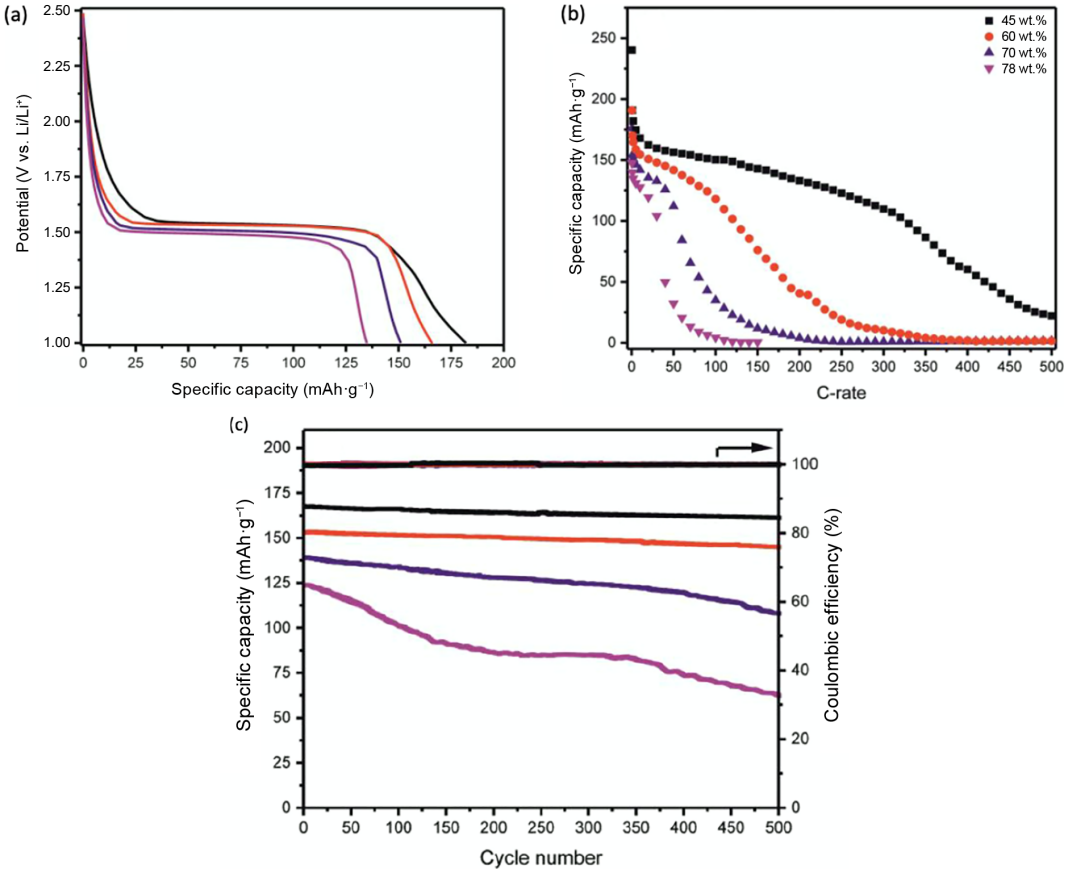

Figure 15 Electrochemical characterizations of VACNT/LTO composites (45 wt.% black, 60 wt.% red, 70 wt.% blue, and 78 wt.% purple). (a) Voltage profiles at 2 C. (b) Discharge capacities at different rates, up to 500 C. (c) Cyclability test at 10 C. Reproduced with permission from Ref. [285], © Elsevier B.V. 2016.

wt.% composites all experienced significant capacity drops at 30, 50, and 100 C, respectively. Contrastingly, the 45 wt.% composites still maintained an impressive high specific capacity of 110 mAh·g^{-1} up to 300 cycles. This, again, was attributed to the LTO particle size and the high VACNT content for improved electronic transport. They also investigated the cyclability of the electrodes at a current density of 10 C. After 500 cycles, the cells exhibited very high-capacity retentions of 97% and 95% for 45 wt.% and 60 wt.% composites and lower capacity retentions of 78% and 51% for the high LTO load composites (70 wt.% and 78 wt.%) (Fig. 15(c)).

Lou et al. [292] reported the electrochemical performance of LIB anodes fabricated by coating manganese oxide (MnO_2) over well-aligned CNTs. The VACNTs were grown on SS foil via a one-step floating catalyst, followed by MnO_2 and carbon coatings by spontaneous deposition and CVD, respectively. The carbon coating was done to prevent the aggregation of the MnO_2 film and to provide more SEI film stability for improved cyclic stability. The C/MnO_2/VACNTs anodes delivered a stable capacity of 738 mAh·g^{-1} at 60 mA·g^{-1} (0.05 C) without any decrease in capacity after 100 cycles and a capacity of 374 mAh·g^{-1} at a high current density of 6000 mA·g^{-1} (5 C). They ascribed the high electrochemical performance of the anodes to the role played by the thin metal oxide film in making the entire composite system active and electrochemically accessible, as well as to the high conductivity, large surface area, and mesoporosity of the VACNTs.

In a more recent report by Abdollahi et al. [43], 3D hierarchical MnO_2 nanoflakes (NFs) were synthesized on VACNTs grown on SS to serve as anodes for LIBs. The SEM and TEM images in Figs. 16(a) and 16(b) show the highly porous MnO_2 NFs, uniformly coated on VACNTs.

To better understand the electrochemical behavior of the composite system, they also fabricated a pristine VACNT anode.

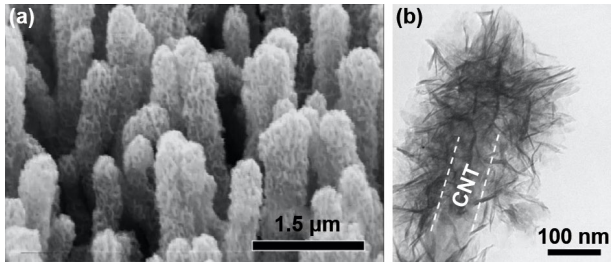

Figure 16 (a) SEM and (b) TEM images of MnO_2 NFs/VACNTs. Reproduced with permission from Ref. [43], © Elsevier Ltd. 2021.

Figures 17(a) and 17(b) show the galvanostatic charge/discharge curves of both electrode materials for the first five cycles. The VACNTs coated with MnO_2 NFs (MnO_2 NFs/VACNTs) composites delivered impressively high first discharge and charge capacities of 2438 and 1289 mAh·g^{-1} at a current density of 250 mA·g^{-1}. In contrast, the pristine VACNT electrode showed notably lower first discharge and charge capacities of 1390 and 533 mAh·g^{-1}, respectively. The anodic peak at 1.3 V and the two marked peaks at 1.04 and 1.63 V (in the first cycle CV curve) in Fig. 17(c) are attributed to the electrolyte decomposition and the formation of the SEI layer. Similarly, the prominent cathodic peaks at 0.67, 1.18, and 1.632 V in Fig. 17(d) are related to the formation of the SEI layer and the reduction of Li^+ ions in the electrolyte with the MnO_2 NFs. Meanwhile, the overlapping redox peaks seen in the first five cycles demonstrate the structural stability and electrochemical reversibility of both electrodes, further confirming the impact of the high mechanical strength of VACNTs.

Upon further cycling, the MnO_2 NFs/VACNTs anode consistently showed superior specific capacities over the pristine VACNT anode, as seen in Fig. 18(a). After 150 cycles, the MnO_2

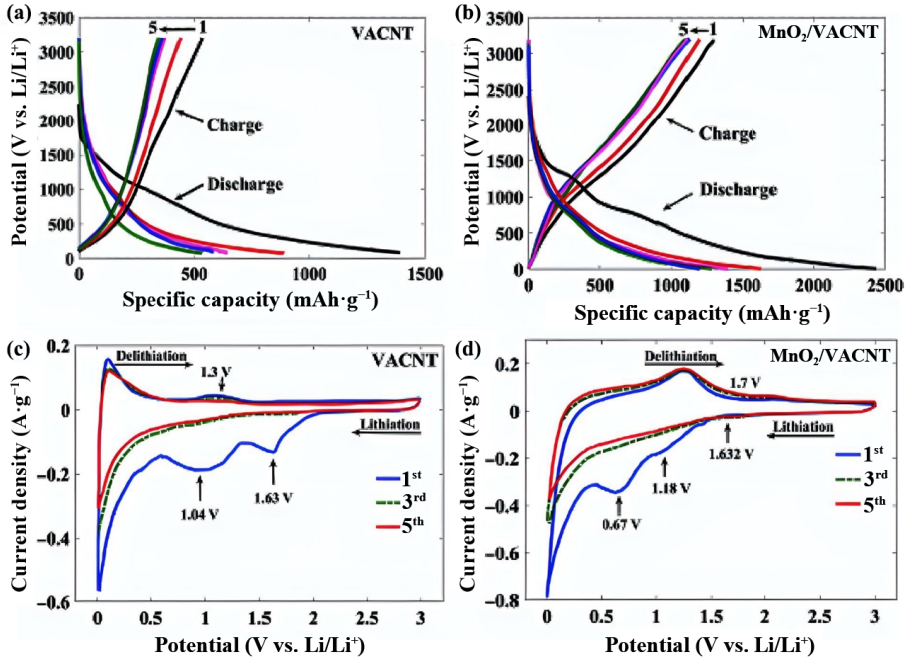

Figure 17 Charge–discharge curves of (a) pristine VACNTs and (b) MnO_2 NFs/VACNTs electrodes. CV curves of the 1st, 3rd, and 5th cycles at a current density of 250 mA·g^{-1} for (c) pristine VACNTs and (d) MnO_2 NFs/VACNTs electrodes. Reproduced with permission from Ref. [43], © Elsevier Ltd. 2021.

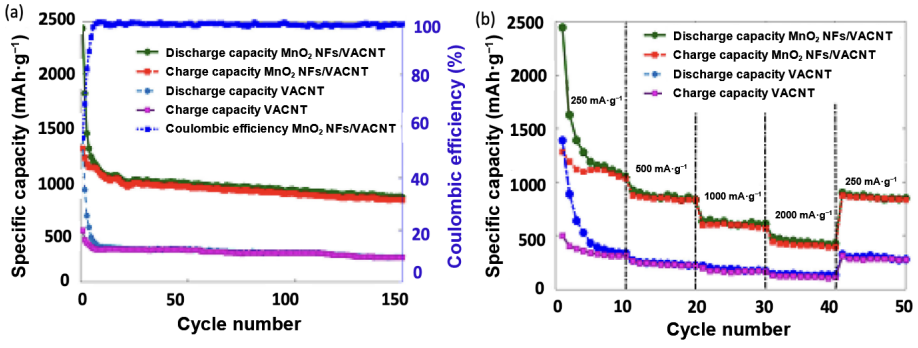

Figure 18 (a) Comparisons between the cycling performance and CE of both pristine and MnO_2 NFs/VACNTs electrodes. (b) Rate capability test of the VACNTs and MnO_2 NFs/VACNTs electrodes. Reproduced with permission from Ref. [43], © Elsevier Ltd. 2021.

NFs/VACNTs electrode still delivered a charge capacity of 803.2 mAh·g^{-1} and increased CE of up to 98.4%. According to Fig. 18(b), the rate capability test results of both electrodes at different current densities (250, 500, 1000, and 2000 mA·g^{-1}) reveal specific capacities of 1115, 849, 601, and 414 mAh·g^{-1}, respectively, for the MnO_2 NFs/VACNTs anode. These results were considerably higher than those observed for the pristine VACNT electrode, with specific capacities of 376, 245, 163, and 109 mAh·g^{-1}. They also reported that the MnO_2 NFs/VACNTs composites exhibited a high electrolyte/electrode contact area, short Li^+ diffusion pathway, and good cyclability. They attributed these outstanding performances to the high electronic conductivity and mechanical strength of the VACNTs to facilitate electron transport and prevent pulverization of the nanostructured electrode.

Luo et al. [293] also reported improved electrochemical performance for Mn_3O_4/SACNT composite anodes. The Mn_3O_4 was anchored on the SACNTs by the decomposition of $Mn(NO_3)_2$. The composite anode displayed high-capacity retention of 95% after 100 cycles at 1 C and a good rate capacity of 342 mAh·g^{-1} at a high current density of 10 C. The SACNTs films provided the conductive pathway and served as a structural framework to anchor the Mn_3O_4 nanoparticles, eliminating the need for a binder and giving room for improved conductivity despite the insulating nature of the Mn_3O_4 particles. The porosity of the Mn_3O_4/SACNTs composites offered by the SACNT films enabled electrolyte infiltration and accommodated the volume change during cycling.

In a very interesting study by Li et al. [294], the electrochemical performance of a ternary anode developed by combining MnO, VACNTs, and TiO_2-C (MnO-CNTs@TiO_2-C) was investigated. Spherical MnO particles were grown along vertically aligned CNTs to produce a sea urchin-like structure (MnO-CNTs) and, afterward, coated with a layer of TiO_2-C. These VACNTs were reported to penetrate the inner MnO core and connect it with the TiO_2-C. This was done to provide an effective route for electron transport and withstand the mechanical strain that occurs during the conversion reaction. Figures 19(a')–19(d') summarize the structural evolution of the MnO-based microsphere anodes upon cycling. The stable TiO_2 shell provided protection for the inner MnO. The carbon coating on the TiO_2 improved the conductivity of the TiO_2 shell and the whole composite anode, giving rise to high reversibility and structural stability. Upon comparing the cycle performance of the four MnO-based anodes over 200 cycles and at a current density of 100 mA·g^{-1}, as expected, the MnO-CNTs@TiO_2-C delivered the highest specific capacity (~ 900 mAh·g^{-1}) amongst the four anodes (Fig. 20(a)). According to Fig. 20(b), the rate capability study of the MnO-CNTs@TiO_2-C anode over 200 cycles revealed high capacities of 825, 720, 623, 524, 449, and 300 mAh·g^{-1} at current densities of 100, 200, 500, 1000, 2000, and 5000 mA·g^{-1}. The result of the cycling test also showed good capacities of 648, 502, and 389 mAh·g^{-1} at high current densities of 100, 1000, and 5000 mA·g^{-1} over 1000, 2000, and 2000 cycles, respectively. As discussed above, excellent

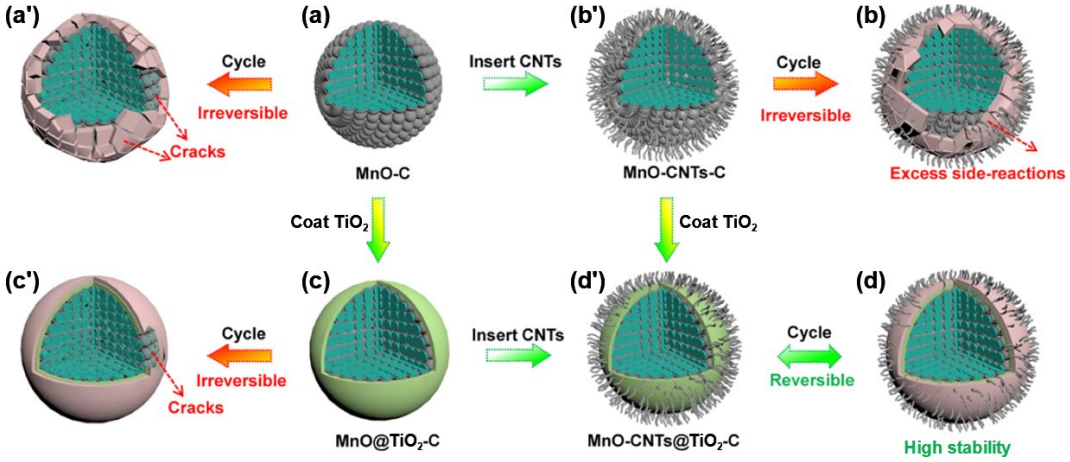

Figure 19 Schematic diagrams of the structural evolution of the MnO-based microsphere anodes upon cycling: ((a) and (a')) MnO-C, ((b) and (b')) MnO-CNTs-C, ((c) and (c')) MnO@TiO_2-C, and ((d) and (d')) MnO-CNTs@TiO_2-C. Reproduced with permission from Ref. [294], © American Chemical Society 2020.

performances were reported because of the combined roles played by the compositing materials.

There are also reports of VACNT/Fe-based composites. For instance, in 2019, Jessl et al. [295] reported the electrochemical performance of a composite anode fabricated by coating VACNTs with α-Fe_2O_3 nanoflakes via a microwave-assisted hydrothermal technique. The VACNT/Fe_2O_3 electrode was cycled at 0.2 C for 50 cycles and after the first 20 cycles, the specific capacity stabilized at a high value of 912 mAh·g^{-1}. A further study of the rate performance revealed that the composite electrode retained more than 400 mAh·g^{-1} after 160 cycles when cycled at 1 C. They attributed this positive behavior to the open structure of the composite electrode and the excellent electronic network offered by the VACNTs. They also investigated the structural stability of the electrode system by disassembling the battery after 40 cycles and taking the SEM images. The SEM images revealed that the initial honeycomb structure of the VACNT/Fe oxide-based composite electrode was maintained, corroborating the usefulness of the VACNT scaffolds.

In another study by Wu et al. [296], improved specific capacities, remarkable capacity retention, and impressive rate capability were reported for composite anodes fabricated by sputtering Fe_3O_4 nanoparticles on SACNT arrays by a one-step direct current (DC) magnetron sputtering technique. The SACNTs, as expected, provided the conducted pathways for electron transport and prevented the agglomeration of the Fe_3O_4 nanoparticles. The SACNT/Fe_3O_4 anode delivered a high specific capacity of over 800 mAh·g^{-1} and CE of more than 90% at 0.1 A·g^{-1} over 100 cycles. At a higher current density of 9 A·g^{-1} (equivalent to 25 C of graphite electrodes), a high specific capacity of 340 mAh·g^{-1} was still achieved after 100 cycles.

Furthermore, pulverization due to volume change during cycling and the poor electronic conductivity suffered by pristine nickel oxide (NiO)-based anodes have been addressed by coating the NiO on VACNT arrays. Susantyoko et al. [297] studied the electrochemical performance of LIB anode fabricated by coating NiO on VA-MWCNTs. The VA-MWCNTs were grown on SS disks via the PECVD technique, and the NiO was sputtered on the VACNT arrays in a DC sputtering chamber. To study the contribution of the VA-MWCNTs to the improved electrochemical performance of the composite anode system, another composite anode was fabricated (SS/NiO) without the VA-MWCNTs on the SS disk. As shown in Fig. 21(a), the VA-MWCNTs/NiO and SS/NiO delivered specific discharge capacities of 864.8 and 285.9 mAh·g^{-1}, respectively, at a fixed current density of 143.6 mA·g^{-1} over 50 cycles. At different charge/discharge rates of 0.1, 0.2, 0.5, and 1 C (1 C = 718 mA·g^{-1}), the VA-MWCNTs/NiO anode delivered specific capacities of 958.2, 936.6, 889.7, and 820.1 mAh·g^{-1}, respectively, whereas the SS/NiO anode delivered low specific capacities of 398.6, 293.7, 215.1, and 159.2 mAh·g^{-1} at the same current densities (Fig. 21(b)). Furthermore, the electrochemical impedance spectroscopy (EIS) results at a low-frequency value of 0.22 Hz were provided, as shown in Fig. 21(c). The resistances of the VA-MWCNTs/NiO anode varied in the range of 62.2 Ω (at 0.6 V discharge) to 228 Ω (2.1 V discharge), whereas the SS/NiO resistances varied largely in the range of 130.8 Ω (at 0.3 V discharge) to 1653.8 Ω (at 3 V charge). Compared to the SS/NiO anode, the VA-MWCNTs/NiO anode displayed lower resistance values across all potentials, indicating better ionic transport. Figure 21(d) reveals that the VA-MWCNTs/NiO anode exhibited lower charge-transfer resistances than the SS/NiO anode across all potential values, resulting in superior electron transport. The excellent rate performance, evidenced by the low internal resistance and the low charge-transfer resistance of the VA-MWCNTs/NiO electrode, was attributed to the improved electronic and ionic transport offered by the presence of the VA-MWCNTs.

The structural stability tests of both anode systems were also performed by disassembling the cells after 50 cycles and taking the SEM images. The images revealed that the active material in the SS/NiO electrode was easily stripped off because of the pulverization of the NiO active material and the poor adhesion of the NiO to the SS disk. Conversely, the structure of the VA-MWCNTs/NiO electrode was maintained. This was attributed to the presence of the VA-MWCNTs as scaffolds to buffer and withstand the mechanical strain caused by volume changes and the strong attachment of the active NiO materials to the VA-MWCNTs. In another study, Deng et al. [298] fabricated a 3D composite anode by coating nitrogen-doped aligned CNT (NACNT) array with NiO nanoparticles wrapped with graphitic carbon layers. The anode system delivered a high specific capacity of 649 mAh·g^{-1}, CE of 95.2%, and capacity retention of 91.6% at 0.2 C over 200 cycles. This excellent performance was also attributed to the role played by the aligned CNTs in improving the electronic conductivity of the active materials and preventing the aggregation of NiO particles.

Aligned CNTs have also been composited with cobalt oxide-based nanoparticles. He et al. [299] investigated the electrochemical performance of an LIB composite anode fabricated by growing Co_3O_4 nanoparticles on SACNT films via the pyrolysis method using $Co(NO_3)_2$ as the precursor. The Co_3O_4/SACNT electrode displayed impressive cycling stability of 910 mAh·g^{-1} after 50 cycles at 0.1 C and great rate performance of 820 mAh·g^{-1} at 1 C. In another study by Liu et al. [300] in 2014,

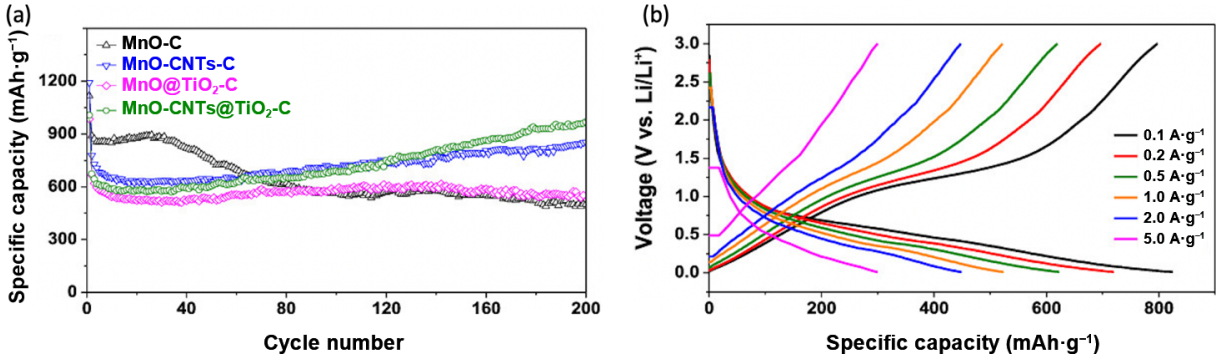

Figure 20 (a) Comparison of the cycling performance of four MnO-based microsphere anodes over 200 cycles at current density of 100 mA·g^{-1}. (b) Rate capability test of the MnO-CNTs@TiO_2-C microsphere anode. Reproduced with permission from Ref. [294], © American Chemical Society 2020.

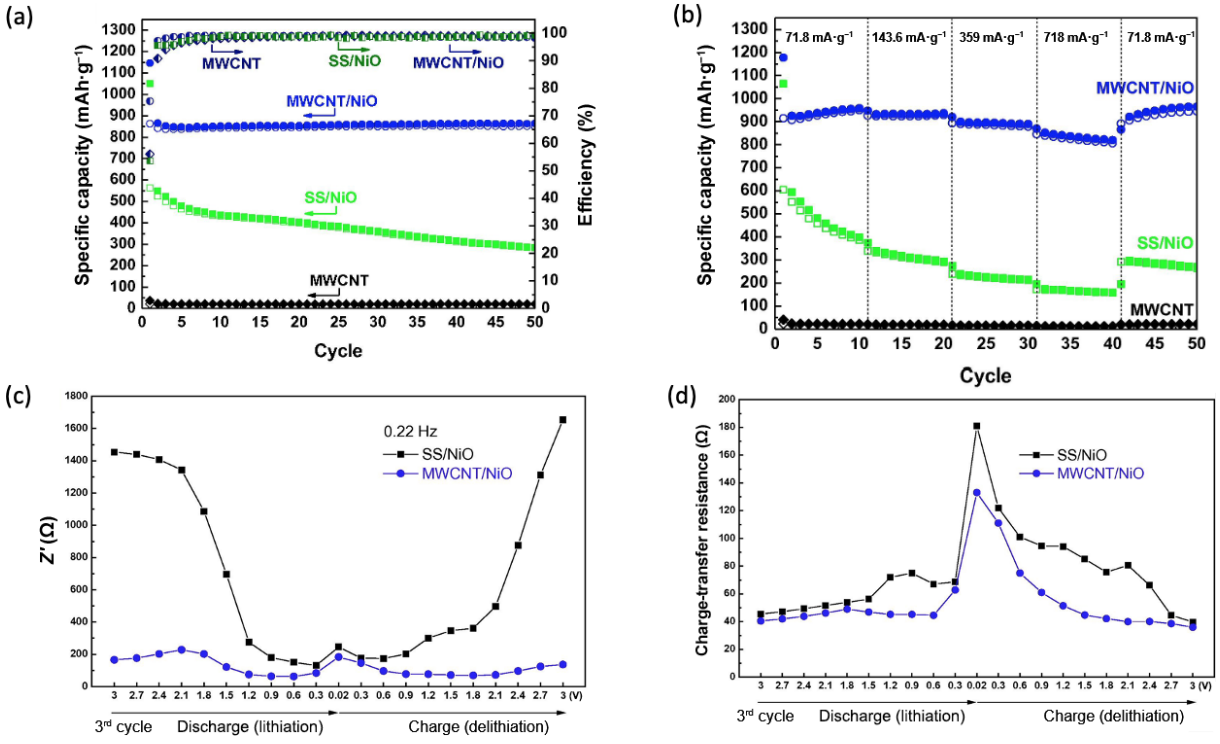

Figure 21 (a) Cycling performance and (b) rate capabilities of MWCNT/NiO, SS/NiO, and MWCNT anodes. (c) Nyquist plots of MWCNT/NiO and SS/NiO anodes, showing the resistance at 0.22 Hz and (d) charge-transfer resistance of MWCNT/NiO and SS/NiO anodes during the 3rd cycle. Reproduced with permission from Ref. [297], © Elsevier Ltd. 2013.

high specific capacity, good rate capability, and impressive cyclability were reported for a 3D VACNTs/$NiCo_2O_4$ core/shell structures electrode. The composite anode system delivered a high and stable reversible specific capacity of 1147.6 mAh·g^{-1} at 100 mA·g^{-1}. At a higher current density of 1000 mA·g^{-1}, the electrode still maintained a high capacity of 712.9 mAh·g^{-1} with no capacity fading over 200 cycles, indicating excellent rate capability and good cycle stability. These two groups attributed the excellent performances of the LIBs to the high conductivity of the aligned CNTs for enhanced electronic transport, the mechanical support provided by the aligned CNTs to buffer volume change during cycling, and the availability of more active sites offered by compositing the different materials together. Table 5 below shows the electrochemical performances of some composite electrodes from other studies.

4 VACNTs-based cathodes for LIBs

As mentioned earlier, the widely used electroactive cathode materials display low electronic conductivities, inhibiting the rate capability of the battery. $LiCoO_2$, $LiFePO_4$, and $LiMn_2O_4$ all exhibit low conductivities of ~ 10^{-4}, ~ 10^{-9}, and ~ 10^{-6} S·cm^{-1}, respectively [302].

Meanwhile, binder-free VACNT arrays grown directly or coated on bare current collectors have been explored as alternatives to improve the conductivities of the electroactive materials and the general electrochemical performance of state-of-the-art cathodes [303]. The intimate electrical contact between current collectors and the active materials reduces the charge transfer resistances. More so, the highly conductive vertical channels of the VACNTs provide faster electronic transport and shorter lithium diffusion pathways, leading to improved rate capabilities in LIBs. Also, there is increased accessibility of Li^+ ions to the electroactive materials due to the large surface area and mesoporous pore sizes of the VACNT arrays. This also ensures faster Li^+ ion diffusion and increased utilization of active materials, thus, leading to high specific capacities.

Ning et al. [304] employed VACNTs, agglomerated CNTs (ACNTs), and carbon black (CB) to construct conductive networks for LFP cathodes. Three different LFP-based cathodes (LFP-VACNT-CB, LFP-ACNT-CB, and LFP-CB) were fabricated, and their electrochemical performances were tested. As shown in Fig. 22, the LFP-VACNT-CB delivered superior discharge capacities at different current densities compared to the other two

Table 5 Electrochemical performances of VACNTs/metal oxide composites from other studies not discussed in the literature

Composite anode	Reversible capacity ($mAh·g^{-1}$)	Capacity retention (%)	Coulombic efficiency (%)	Current density ($mA·g^{-1}$)	Number of cycles	References
SACNT/TiO_2	> 100	—	~ 100	30 C	2500	[301]
SACNT/$Li_4Ti_5O_{12}$	154.7	89	~ 100	5 C	1200	[286]
VACNTs/MnO_2	738	99.9	—	60	100	[292]
VACNTs/$NiCo_2O_4$ core	712.9	—	—	1000	200	[300]
SACNTs/SnO_2	1004	—	96	0.1 C	80	[225]

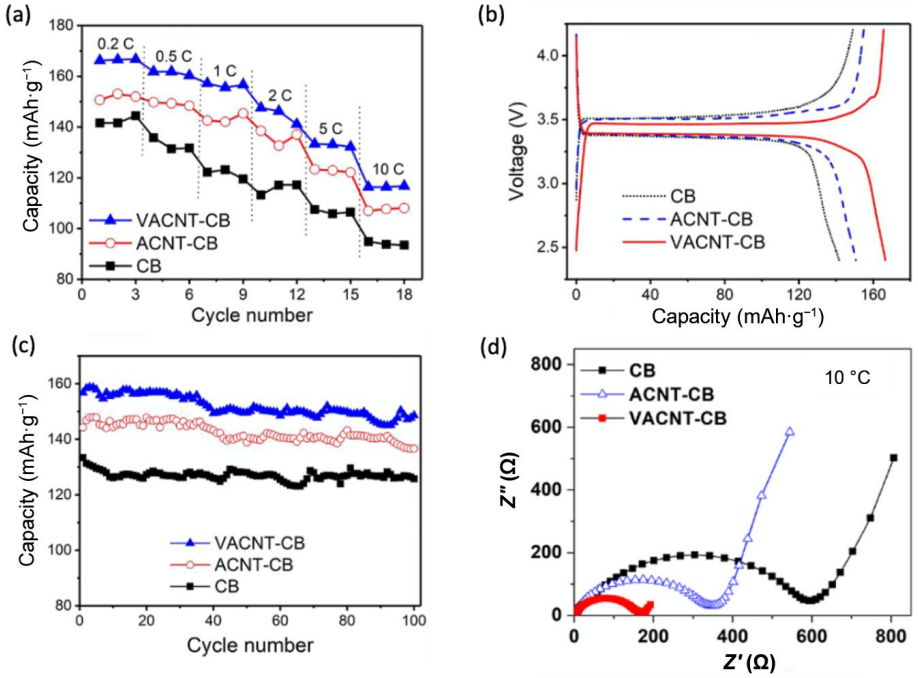

Figure 22 (a) Rate capability, (b) charge–discharge curves at 0.2 C, (c) cycling performances at 1 C, and (d) impedance curves at 10 °C of LFP-VACNT-CB, LFP-ACNT-CB, and LFP-CB cathodes. Reproduced with permission from Ref. [304], © Elsevier Ltd. 2018.

electrodes, an evidence of excellent rate capability. The extended charge–discharge platform at ~ 3.4 V in Fig. 22(b), observed for the LFP-VACNT-CB cathode, is indicative of the involvement of more electroactive materials in the cycling process due to the larger surface area and the mesoporous pore geometry of VACNT arrays described earlier. The LFP-VACNT-CB cathode also showed better specific capacity and capacity retention after 100 cycles at 1 C (1 C = 140 $mAh·g^{-1}$), as shown in Fig. 22(c). The impedance curves at 10 °C for the three electrodes shown in Fig. 22(d) reveal a significantly reduced charge transfer resistance (corresponding to the smaller width of the semicircle) for the LFP-VACNT-CB cathode. This was attributed to the superior conductivity offered by the VACNTs.

Ventrapragada et al. [198] attempted to reduce the resistance at the current collector and active material interface (CCAMI) by coating VACNTs with electrochemically active LFP powders. The electrode delivered an impressively high energy density of ~ 500 $Wh·kg^{-1}$ at ~ 170 $W·kg^{-1}$. The electrode was also reported to have withstood a very high current density of ~ 600 $mA·g^{-1}$ for 500 cycles. The high electrical conductivity offered by the VACNT arrays allowed for highly improved electron transport across the CCAMI. The excellent rate capability was also attributed to the high stability of the VACNTs. Yilmaz et al. [305] fabricated a 3D cathode consisting of an Al current collector, micropatterned VACNT arrays, and LFP powders coated on the VACNTs via electrophoretic deposition technique. As expected, the highly conductive VACNT cores offered a high specific surface area to facilitate more significant mass loading of the electroactive LFP powders, resulting in a high specific capacity of 143 $mAh·g^{-1}$ at C/20. Using a simple ultrasonication technique, Luo et al. [306] fabricated a binder-free $LiCoO_2$-SACNT cathode. The electrode delivered a specific discharge capacity of 151 $mAh·g^{-1}$ at 0.1 C after 50 cycles and a high specific capacity of over 130 $mAh·g^{-1}$ at 2 C. The SACNTs were reported to have provided a continuous network and porous channels for the rapid transport of electrons and improved Li^+ ions accessibility.

VACNTs have also been directly employed in the fabrication of V_2O_5-VACNTs composite cathodes with high specific capacities and excellent rate capabilities. Lu et al. [201] investigated the electrochemical properties of a V_2O_5-VACNTs cathode fabricated by coating VACNTs with coaxial layers of V_2O_5. The cathode delivered a high capacity of 368 $mAh·g^{-1}$ alongside an excellent rate capability. Jiang et al. [40] designed a poly(3,4-ethylenedioxythiophene):polystyrenesulfonic acid (PEDOT)-coated hierarchical free-standing V_2O_5-VACNTs-graphene foam (GF) porous cathode. The electrode exhibited a high reversible capacity of 296.8 $mAh·g^{-1}$ and excellent capacity retention of 113.3 $mAh·g^{-1}$ at 5 C after 1000 cycles. They also performed first-principles calculations to ascertain the contribution of the VACNTs in the electrochemical performance of the composite cathode. The result of their calculation confirmed that the presence of the VACNTs in the structure enhanced electronic conductivity and Li^+ adsorption, which led to the impressive Li^+ ion storage and conversion behavior observed in the cathode.

5 Conclusions and prospects

In this article, we reviewed the electrochemical performances of

vertically aligned CNTs and their composites in LIBs. Compared to the randomly aligned CNTs, VACNTs offer improved electrochemical performance in LIBs. They possess ultrahigh electronic conductivity, which reduces electron transfer resistance. Their regular pore structure and unidirectionality provide improved electrolyte access, lower ion-diffusion resistance, and shorter and directional pathways for enhanced and continuous transport of Li^+ ions, which are key requirements for fast electrode kinetics. More so, the extremely large surface area provided by the VACNTs increases the number of Li^+ ions that could be stored in the electrode, leading to an improved specific capacity. Regardless of the huge irreversible capacity loss observed in the VACNT-based anodes, they are still preferable to conventional graphitic anodes due to their superior mechanical property, electrical conductivity, large aspect ratio, chemical stability, structural flexibility, and reduced tortuosity. When used as support in composite systems, their mesoporous nature and unique mechanical properties offer sufficient voids to withstand the volumetric changes that occur during cycling and obviate pulverization. They also form highly conductive networks, which can potentially enhance the electrical contact between the electroactive materials. This leads to remarkably improved cyclability and rate capability.

Meanwhile, owing to the growing demands for incorporating CNTs in LIBs, there are still a lot that need to be done in this field for these materials to reach their full potential in the battery industry. For instance, there is a need to develop new or optimize the available synthesis and purification methods for adequate and high yield of CNTs. VACNTs directly synthesized on current collectors (e.g., copper, aluminum, stainless steel, and nickel) without any intermediate layer appear to be highly promising for enhanced electrochemical performances in future LIBs. So, there is a need to develop facile techniques for growing large-scale and high-quality VACNTs directly on these current collectors at low cost.

Furthermore, there is a need to employ both experimental and theoretical (such as *ab initio* molecular dynamics simulations based on density functional theory) frameworks to properly understand the lithium storage mechanisms in CNTs. Again, the impacts of different CNT structures and morphologies (length, diameter, number of walls, defects, and alignment) on the general electrochemical performance of LIBs remain unclear. Thus, it is paramount to carry out both *ab initio* and empirical studies in this regard to better understand and correlate the battery performance with the CNT properties. This would allow for a more controlled and efficient synthesis of CNTs with desired properties.

More so, regardless of the improved specific energy density offered by VACNTs and their various composites, there is still the issue of low volumetric energy density resulting from the reduced mass of the active materials, which are in the nanoscale range. Thus, attention should be drawn, and efforts channeled towards simultaneously increasing the mass loading of electrodes and maintaining high active material use.

Lastly, despite the improved battery performances reported in this review for the aligned CNTs composite electrodes, there are still some issues hindering their commercialization, such as poor adhesion of nanoparticles with VACNTs, agglomeration of active materials, choice of composite materials, cost, fabrication techniques, and inadequate understanding of the surface chemistry in the composite system. Hence, there is a need for more extensive research for these issues to be addressed. In the case of choice of composite materials, owing to the increase in demand for LIBs, it is essential to choose cheap and heavily abundant materials, such as Si, Sn, and Fe. There is also a need to understand better the extent of interactions between the VACNTs and the compositing materials. Since the electrochemical process involves the transfer of electrons and ions, a clear understanding of the impact of the VACNT interactions with the active materials on the surface charge transfer is important. More so, efforts should be made towards developing facile, environmentally friendly, and cost-effective fabrication techniques to achieve commercialization of these nanostructured composite electrodes.

Acknowledgment

This work was supported by the National Science Foundation of the United States (Nos. 1506640, 2134375, and 2213923). We would like to express our gratitude to Dr. Arun Thapa for his invaluable inputs during the revision of the article.

References

[1] Hudak, N. S. Nanostructured electrode materials for lithium-ion batteries. In *Lithium-ion Batteries*; Pistoia, G., Ed.; Elsevier: Oxford, 2014; pp 57–82.

[2] Bruce, P. G.; Scrosati, B.; Tarascon, J. M. Nanomaterials for rechargeable lithium batteries. *Angew. Chem., Int. Ed.* **2008**, *47*, 2930–2946.

[3] Pomerantseva, E.; Bonaccorso, F.; Feng, X. L.; Cui, Y.; Gogotsi, Y. Energy storage: The future enabled by nanomaterials. *Science* **2019**, *366*, eaan8285.

[4] Baldwin, R. S.; Wu, J.; Bennett, W. Nanomaterials for advanced lithium-ion battery anodes. In *Advanced Nanomaterials for Aerospace Applications*; Cabrera, C. R.; Miranda, F., Eds.; Jenny Stanford Publishing: New York, 2014; pp 131–147.

[5] Majdi, H. S.; Latipov, Z. A.; Borisov, V.; Yuryevna, N. O.; Kadhim, M. M.; Suksatan, W.; Khlewee, I. H.; Kianfar, E. Nano and battery anode: A review. *Nanoscale Res. Lett.* **2021**, *16*, 177.

[6] Sun, Z. H.; Shu, M.; Li, J. B.; Liu, B.; Yao, H. Y.; Guan, S. W.; Sun, Z. H. Carbon nanotube-hyperbranched polymer core–shell nanowires with highly accessible redox-active sites for fast-charge organic lithium batteries. *J. Energy Chem.* **2023**, *78*, 30–36.

[7] Darkwa, K. M.; Ampong, D. N.; Boamah, R.; Akromah, S.; Amedalor, R.; Agyei-Tuffour, B.; Dodoo-Arhin, D.; Goosen, N. J.; Gupta, R. K. Nanowires for electrochemical energy storage applications. *Nanowires* **2023**, 113–134.

[8] Wang, G. X.; Shen, X. P.; Yao, J.; Park, J. Graphene nanosheets for enhanced lithium storage in lithiumion batteries. *Carbon* **2009**, *47*, 2049–2053.

[9] Mo, R. W.; Tan, X. Y.; Li, F.; Tao, R.; Xu, J. H.; Kong, D. J.; Wang, Z. Y.; Xu, B.; Wang, X.; Wang, C. M. et al. Tin-graphene tubes as anodes for lithium-ion batteries with high volumetric and gravimetric energy densities. *Nat. Commun.* **2020**, *11*, 1374.

[10] Mu, Y. B.; Han, M. S.; Li, J. Y.; Liang, J. B.; Yu, J. Growing vertical graphene sheets on natural graphite for fast charging lithium-ion batteries. *Carbon* **2021**, *173*, 477–484.

[11] Tian, M. Y.; Ben, L.; Jin, Z.; Ji, H. X.; Yu, H. L.; Zhao, W. W.; Huang, X. J. Excellent low-temperature electrochemical cycling of an anode consisting of Si nanoparticles seeded in Sn nanowires for lithium-ion batteries. *Electrochim. Acta* **2021**, *396*, 139224.

[12] Nam, K. T.; Kim, D.; Yoo, P. J.; Chiang, C.; Meethong, N.; Hammond, P. T.; Chiang, Y.; Belcher, A. M. Virus-enabled synthesis and assembly of nanowires for lithium ion battery electrodes. *Science* **2006**, *80*, 885–888.

[13] Zhong, Y.; Deng, K.; Zheng, J.; Zhang, T. T.; Liu, P.; Lv, X. B.; Tian, W.; Ji, J. Y. One-step growth of the interconnected carbon nanotubes/graphene hybrids from cuttlebone-derived bi-functional catalyst for lithium-ion batteries. *J. Mater. Sci. Technol.* **2023**, *149*, 205–213.

[14] Chen, T.; Liu, B. C.; Zheng, M. L.; Luo, Y. S. Suspensions based on $LiFePO_4$/carbon nanotubes composites with three-dimensional conductive network for lithium-ion semi-solid flow batteries. *J. Energy Storage* **2023**, *57*, 106300.

[15] Zhang, M. M.; Chen, J. Y.; Li, H.; Wang, C. R. Recent progress in Li-ion batteries with TiO_2 nanotube anodes grown by

electrochemical anodization. *Rare Met.* **2021**, *40*, 249–271.
[16] Yin, H.; Li, Q. W.; Cao, M. L.; Zhang, W.; Zhao, H.; Li, C.; Huo, K. F.; Zhu, M. Q. Nanosized-bismuth-embedded 1D carbon nanofibers as high-performance anodes for lithium-ion and sodium-ion batteries. *Nano Res.* **2017**, *10*, 2156–2167.
[17] Zhang, T.; Qiu, D. P.; Hou, Y. L. Free-standing and consecutive ZnSe@carbon nanofibers architectures as ultra-long lifespan anode for flexible lithium-ion batteries. *Nano Energy.* **2022**, *94*, 106909.
[18] Yu, S. X.; Guo, B. B.; Zeng, T. B.; Qu, H. Q.; Yang, J. L.; Bai, J. M. Graphene-based lithium-ion battery anode materials manufactured by mechanochemical ball milling process: A review and perspective. *Compos. Part B: Eng.* **2022**, *246*, 110232.
[19] Sun, X.; Yang, C. K.; Zhao, Y. J.; Li, Y.; Shang, Z. C.; Zhou, H. H.; Liu, W.; Luo, L.; Sun, X. M. Ultrathin aluminum nanosheets grown on carbon nanotubes for high performance lithium Ion batteries. *Adv. Funct. Mater.* **2022**, *32*, 2109112.
[20] Chang, C. B.; Tsai, C. Y.; Chen, K. T.; Tuan, H. Y. Solution-grown phosphorus-hyperdoped silicon nanowires/carbon nanotube bilayer fabric as a high-performance lithium-ion battery anode. *ACS Appl. Energy Mater.* **2021**, *4*, 3160–3168.
[21] Shi, J.; Jiang, X. S.; Ban, B. Y.; Li, J. W.; Chen, J. Carbon nanotubes-enhanced lithium storage capacity of recovered silicon/carbon anodes produced from solar-grade silicon kerf scrap. *Electrochim. Acta* **2021**, *381*, 138269.
[22] Tian, F.; Nie, W.; Zhong, S. W.; Liu, X. L.; Tang, X. D.; Zhou, M. M.; Guo, Q. K.; Hu, S. Highly ordered carbon nanotubes to improve the conductivity of $LiNi_{0.8}Co_{0.15}Al_{0.05}O_2$ for Li-ion batteries. *J. Mater. Sci.* **2020**, *55*, 12082–12090.
[23] Gupta, N.; Gupta, S. M.; Sharma, S. K. Carbon nanotubes: Synthesis, properties, and engineering applications. *Carbon Lett.* **2019**, *29*, 419–447.
[24] Inoue, Y.; Hayashi, K.; Karita, M.; Nakano, T.; Shimamura, Y.; Shirasu, K.; Yamamoto, G.; Hashida, T. Study on the mechanical and electrical properties of twisted CNT yarns fabricated from CNTs with various diameters. *Carbon* **2021**, *176*, 400–410.
[25] Okwundu, O. S.; Aniekwe, E. U.; Nwanno, C. E. Unlimited potentials of carbon: Different structures and uses (a review). *Metall. Mater. Eng.* **2018**, *24*, 145–171.
[26] Hsia, B.; Marschewski, J.; Wang, S.; In, J. B.; Carraro, C.; Poulikakos, D.; Grigoropoulos, C. P.; Maboudian, R. Highly flexible, all solid-state micro-supercapacitors from vertically aligned carbon nanotubes. *Nanotechnology* **2014**, *25*, 055401.
[27] Reit, R.; Nguyen, J.; Ready, W. J. Growth time performance dependence of vertically aligned carbon nanotube supercapacitors grown on aluminum substrates. *Electrochim. Acta.* **2013**, *91*, 96–100.
[28] Wang, X. H.; Sun, L. M.; Susantyoko, R. A.; Fan, Y.; Zhang, Q. Ultrahigh volumetric capacity lithium ion battery anodes with CNT-Si film. *Nano Energy* **2014**, *8*, 71–77.
[29] Sun, L. M.; Wang, X. H.; Wang, Y. R.; Zhang, Q. Roles of carbon nanotubes in novel energy storage devices. *Carbon* **2017**, *122*, 462–474.
[30] Huang, S.; Du, X. F.; Ma, M. B.; Xiong, L. L. Recent progress in the synthesis and applications of vertically aligned carbon nanotube materials. *Nanotechnol. Rev.* **2021**, *10*, 1592–1623.
[31] Sharma, P.; Pavelyev, V.; Kumar, S.; Mishra, P.; Islam, S. S.; Tripathi, N. Analysis on the synthesis of vertically aligned carbon nanotubes: Growth mechanism and techniques. *J. Mater. Sci. Mater. Electr.* **2020**, *31*, 4399–4443.
[32] Abdollahi, A.; Abnavi, A.; Ghasemi, S.; Mohajerzadeh, S.; Sanaee, Z. Flexible free-standing vertically aligned carbon nanotube on activated reduced graphene oxide paper as a high performance lithium ion battery anode and supercapacitor. *Electrochim. Acta.* **2019**, *320*, 134598.
[33] Welna, D. T.; Qu, L. T.; Taylor, B. E.; Dai, L. M.; Durstock, M. F. Vertically aligned carbon nanotube electrodes for lithium-ion batteries. *J. Power Sources* **2011**, *196*, 1455–1460.
[34] Futaba, D. N.; Hata, K.; Yamada, T.; Hiraoka, T.; Hayamizu, Y.; Kakudate, Y.; Tanaike, O.; Hatori, H.; Yumura, M.; Iijima, S. Shape-engineerable and highly densely packed single-walled carbon nanotubes and their application as super-capacitor electrodes. *Nat. Mater.* **2006**, *5*, 987–994.
[35] Honda, Y.; Haramoto, T.; Takeshige, M.; Shiozaki, H.; Kitamura, T.; Ishikawa, M. Aligned MWCNT sheet electrodes prepared by transfer methodology providing high-power capacitor performance. *Electrochem. Solid-State Lett.* **2007**, *10*, A106–A110.
[36] Ngo, T. D. Introduction to composite materials. In *Composite and Nanocomposite Materials - From Knowledge to Industrial Applications*; Ngo, T. D., Ed.; IntechOpen 2020
[37] Kasavajjula, U.; Wang, C. S.; Appleby, A. J. Nano- and bulk-silicon-based insertion anodes for lithium-ion secondary cells. *J. Power Sources* **2007**, *163*, 1003–1039.
[38] Wang, W.; Epur, R.; Kumta, P. N. Vertically aligned silicon/carbon nanotube (VASCNT) arrays: Hierarchical anodes for lithium-ion battery. *Electrochem. Commun.* **2011**, *13*, 429–432.
[39] Li, S. S.; Luo, Y. H.; Lv, W.; Yu, W. J.; Wu, S. D.; Hou, P. X.; Yang, Q. H.; Meng, Q. B.; Liu, C.; Cheng, H. M. Vertically aligned carbon nanotubes grown on graphene paper as electrodes in lithium-ion batteries and dye-sensitized solar cells. *Adv. Energy Mater.* **2011**, *1*, 486–490.
[40] Jiang, H. F.; Wei, Z. X.; Cai, X. Y.; Lai, L. F.; Ma, J. M.; Huang, W. A cathode for Li-ion batteries made of vanadium oxide on vertically aligned carbon nanotube arrays/graphene foam. *Chem. Eng. J.* **2019**, *359*, 1668–1676.
[41] Dörfler, S.; Hagen, M.; Althues, H.; Tübke, J.; Kaskel, S.; Hoffmann, M. J. High capacity vertical aligned carbon nanotube/sulfur composite cathodes for lithium-sulfur batteries. *Chem. Commun.* **2012**, *48*, 4097–4099.
[42] Li, X. L.; Zhang, J. X.; Qi, G. C.; Cheng, J. L.; Wang, B. Vertically aligned N-doped carbon nanotubes arrays as efficient binder-free catalysts for flexible Li-CO_2 batteries. *Energy Storage Mater.* **2021**, *35*, 148–156.
[43] Abdollahi, A.; Abnavi, A.; Ghasemi, F.; Ghasemi, S.; Sanaee, Z.; Mohajerzadeh, S. Facile synthesis and simulation of MnO_2 nanoflakes on vertically aligned carbon nanotubes, as a high-performance electrode for Li-ion battery and supercapacitor. *Electrochim. Acta.* **2021**, *390*, 138826.
[44] Zou, Q. M.; Deng, L. M.; Li, D. W.; Zhou, Y. S.; Golgir, H. R.; Keramatnejad, K.; Fan, L. S.; Jiang, L.; Silvain, J. F.; Lu, Y. F. Thermally stable and electrically conductive, vertically aligned carbon nanotube/silicon infiltrated composite structures for high-temperature electrodes. *ACS Appl. Mater. Interfaces* **2017**, *9*, 37340–37349.
[45] Hahm, M. G.; Hashim, D. P.; Vajtai, R.; Ajayan, P. M. A review: Controlled synthesis of vertically aligned carbon nanotubes. *Carbon Lett.* **2011**, *12*, 185–193.
[46] Liu, Q. X.; Shi, X. F.; Jiang, Q. Y.; Li, R.; Zhong, S.; Zhang, R. F. Growth mechanism and kinetics of vertically aligned carbon nanotube arrays. *EcoMat.* **2021**, *3*, e12118.
[47] Gangele, A.; Sharma, C. S.; Pandey, A. K. Synthesis of patterned vertically aligned carbon nanotubes by PECVD using different growth techniques: A review. *J. Nanosci. Nanotechnol.* **2017**, *17*, 2256–2273.
[48] Shi, W. B.; Plata, D. L. Vertically aligned carbon nanotubes: Production and applications for environmental sustainability. *Green Chem.* **2018**, *20*, 5245–5260.
[49] Wang, X.; Wang, T. Y.; Borovilas, J.; He, X. D.; Du, S. Y.; Yang, Y. Vertically-aligned nanostructures for electrochemical energy storage. *Nano Res.* **2019**, *12*, 2002–2017.
[50] Zhang, Q.; Huang, J. Q.; Zhao, M. Q.; Qian, W. Z.; Wei, F. Carbon nanotube mass production: Principles and processes. *ChemSusChem* **2011**, *4*, 864–889.
[51] Schmid, G. *Nanoparticles*: *From Theory to Application*; Wiley-VCH Verlag GmbH & Co. KGaA: Weinheim, 2003
[52] Su, F. B.; Zhao, X. S.; Wang, Y.; Zeng, J. H.; Zhou, Z. C.; Lee, J. Y. Synthesis of graphitic ordered macroporous carbon with a three-dimensional interconnected pore structure for electrochemical applications. *J. Phys. Chem. B.* **2005**, *109*, 20200–20206.
[53] Tomar, R.; Abdala, A. A.; Chaudhary, R. G.; Singh, N. B. Photocatalytic degradation of dyes by nanomaterials. *Mater. Today Proc.* **2020**, *29*, 967–973.
[54] Leslie-Pelecky, D. L.; Rieke, R. D. Magnetic properties of

nanostructured materials. *Chem. Mater.* **1996**, *8*, 1770–1783.
[55] Krishnan, S. K.; Singh, E.; Singh, P.; Meyyappan, M.; Nalwa, H. S. A review on graphene-based nanocomposites for electrochemical and fluorescent biosensors. *RSC Adv.* **2019**, *9*, 8778–8881.
[56] Geoffrion, L. D.; Guisbiers, G. Quantum confinement: Size on the grill! *J. Phys. Chem. Solids* **2020**, *140*, 109320.
[57] Wu, Q.; Miao, W. S.; Zhang, Y. D.; Gao, H. J.; Hui, D. Mechanical properties of nanomaterials: A review. *Nanotechnol. Rev.* **2020**, *9*, 259–273.
[58] Lai, C. M.; Lia, L. Y.; Luo, B. Y.; Shen, J. W.; Shao, J. W. Current advances and prospects in carbon nanomaterials-based drug deliver systems for cancer therapy. *Curr. Med. Chem.* **2023**, *30*, 2710–2733.
[59] Khorsandi, Z.; Borjian-Boroujeni, M.; Yekani, R.; Varma, R. S. Carbon nanomaterials with chitosan: A winning combination for drug delivery systems. *J. Drug Deliv. Sci. Technol.* **2021**, *66*, 102847.
[60] Li, Z.; Xu, K.; Qin, L. L.; Zhao, D. C.; Yang, N. L.; Wang, D.; Yang, Y. Hollow nanomaterials in advanced drug delivery systems: From single-to multiple shells. *Adv. Mater.* **2022**, *35*, 2203890.
[61] Alipour, A.; Gholami, A.; Kalashgrani, Y. Nano protein and peptides for drug delivery and anticancer agents. *J. Adv. Appl. NanoBio-Technol.* **2022**, *3*, 60–64.
[62] Zhang, Q. F.; Uchaker, E.; Candelaria, S. L.; Cao, G. Z. Nanomaterials for energy conversion and storage. *Chem. Soc. Rev.* **2013**, *42*, 3127–3171.
[63] Liu, X. H.; Zhong, L.; Huang, S.; Mao, S. X.; Zhu, T.; Huang, J. Y. Size-dependent fracture of silicon nanoparticles during lithiation. *ACS Nano* **2012**, *6*, 1522–1531.
[64] Manthiram, A.; Murugan, A. V.; Sarkar, A.; Muraliganth, T. Nanostructured electrode materials for electrochemical energy storage and conversion. *Energy Environ. Sci.* **2008**, *1*, 621–638.
[65] Gan, Z. H.; Yin, J. Y.; Xu, X.; Cheng, Y. H.; Yu, T. Nanostructure and advanced energy storage: Elaborate material designs lead to high-rate pseudocapacitive ion storage. *ACS Nano.* **2022**, *16*, 5131–5152.
[66] Chen, J. M.; Lin, Y. P.; Wang, H.; Li, J. M.; Liu, S. J.; Lee, J.-M.; Zhao, Q. 2D molybdenum compounds for electrocatalytic energy conversion. *Adv. Funct. Mater.* **2023**, *33*, 2210236.
[67] Shahid, M.; Javed, H. M. A.; Ahmad, M. I.; Qureshi, A. A.; Khan, M. I.; Alnuwaiser, M. A.; Ahmed, A.; Khan, M. A.; Tag-ElDin, E. S. M.; Shahid, A. et al. A brief assessment on recent developments in efficient electrocatalytic nitrogen reduction with 2D non-metallic nanomaterials. *Nanomaterials (Basel)* **2022**, *12*, 3413.
[68] Li, Z. J.; Zhai, L.; Ge, Y. Y.; Huang, Z. Q.; Shi, Z. Y.; Liu, J. W.; Zhai, W.; Liang, J. Z.; Zhang, H. Wet-chemical synthesis of two-dimensional metal nanomaterials for electrocatalysis. *Natl. Sci. Rev.* **2022**, *9*, nwab142.
[69] Liu, Y. Y.; Wang, Y. H.; Zhao, S. L.; Tang, Z. Y. Metal-organic framework-based nanomaterials for electrocatalytic oxygen evolution. *Small Methods* **2022**, *6*, 2200773.
[70] Eivazzadeh-Keihan, R.; Noruzi, E. B.; Chidar, E.; Jafari, M.; Davoodi, F.; Kashtiaray, A.; Gorab, M. G.; Hashemi, S. M.; Javanshir, S.; Cohan, R. A. et al. Applications of carbon-based conductive nanomaterials in biosensors. *Chem. Eng. J.* **2022**, *442*, 136183.
[71] Song, F. X.; Xu, X. J.; Ding, H. Z.; Yu, L.; Huang, H. C.; Hao, J. T.; Wu, C. H.; Liang, R.; Zhang, S. H. Recent progress in nanomaterial-based biosensors and theranostic nanomedicine for bladder cancer. *Biosensors (Basel)* **2023**, *13*, 106.
[72] Holzinger, M.; Le Goff, A.; Cosnier, S. Nanomaterials for biosensing applications: A review. *Front. Chem.* **2014**, *2*, 63.
[73] Yang, G. H.; Liu, F. L.; Zhao, J. Y.; Fu, L. J.; Gu, Y. Q.; Qu, L. L.; Zhu, C. Z.; Zhu, J. J.; Lin, Y. H. MXenes-based nanomaterials for biosensing and biomedicine. *Coord. Chem. Rev.* **2023**, *479*, 215002.
[74] Shahid-Ul-Islam; Bairagi, S.; Kamali, M. R. Review on green biomass-synthesized metallic nanoparticles and composites and their photocatalytic water purification applications: Progress and perspectives. *Chem. Eng. J. Adv.* **2023**, *14*, 100460.
[75] Yu, S. J.; Tang, H.; Zhang, D.; Wang, S. Q.; Qiu, M. Q.; Song, G.; Fu, D.; Hu, B. W.; Wang, X. K. MXenes as emerging nanomaterials in water purification and environmental remediation. *Sci. Total Environ.* **2022**, *811*, 152280.
[76] Singh, K. K.; Singh, A.; Rai, S. A study on nanomaterials for water purification. *Mater. Today Proc.* **2022**, *51*, 1157–1163.
[77] Savage, N.; Diallo, M. S. Nanomaterials and water purification: Opportunities and challenges. *J. Nanopart. Res.* **2005**, *7*, 331–342.
[78] Rahman, M. A.; Song, G. S.; Bhatt, A. I.; Wong, Y. C.; Wen, C. E. Nanostructured silicon anodes for high-performance lithium-ion batteries. *Adv. Funct. Mater.* **2016**, *26*, 647–678.
[79] Ge, M. Z.; Cao, C. Y.; Biesold, G. M.; Sewell, C. D.; Hao, S. M.; Huang, J. Y.; Zhang, W.; Lai, Y. K.; Lin, Z. Q. Recent advances in silicon-based electrodes: From fundamental research toward practical applications. *Adv. Mater.* **2021**, *33*, 2004577.
[80] Wu, H.; Cui, Y. Designing nanostructured Si anodes for high energy lithium ion batteries. *Nano Today* **2012**, *7*, 414–429.
[81] Guo, Y. G.; Hu, J. S.; Wan, L. J. Nanostructured materials for electrochemical energy conversion and storage devices. *Adv. Mater.* **2008**, *20*, 2878–2887.
[82] Jiao, F.; Bruce, P. G. Mesoporous crystalline β-MnO_2-A reversible positive electrode for rechargeable lithium batteries. *Adv. Mater.* **2007**, *19*, 657–660.
[83] Kukovecz, Á.; Kozma, G.; Konya, Z. Multi-walled carbon nanotubes. In *Springer Handbook of Nanomaterials*; Vajtai, R., Ed.; Springer: Berlin Heidelberg, 2013; pp. 147–188.
[84] Zhu, S.; Sheng, J.; Chen, Y.; Ni, J. F.; Li, Y. Carbon nanotubes for flexible batteries: Recent progress and future perspective. *Natl. Sci. Rev.* **2021**, *8*, nwaa261.
[85] Tîlmaciu, C. M.; Morris, M. C. Carbon nanotube biosensors. *Front. Chem.* **2015**, *3*, 59.
[86] Thostenson, E. T.; Ren, Z. F.; Chou, T. W. Advances in the science and technology of carbon nanotubes and their composites: A review. *Compos. Sci. Technol.* **2001**, *61*, 1899–1912.
[87] Lin, C. T.; Lee, C. Y.; Chin, T. S.; Xiang, R.; Ishikawa, K.; Shiomi, J.; Maruyama, S. Anisotropic electrical conduction of vertically-aligned single-walled carbon nanotube films. *Carbon* **2011**, *49*, 1446–1452.
[88] Ganesh, E. N. Single walled and multi walled carbon nanotube structure, synthesis and applications. *Int. J. Innov. Technol. Explor. Eng.* **2013**, *2*, 311–320.
[89] Devi, R.; Gill, S. S. A squared bossed diaphragm piezoresistive pressure sensor based on CNTs for low pressure range with enhanced sensitivity. *Microsyst. Technol.* **2021**, *27*, 3225–3233.
[90] Baughman, R. H.; Zakhidov, A. A.; De Heer, W. A. Carbon nanotubes—The route toward applications. *Science* **2002**, *297*, 787–792.
[91] Spitalsky, Z.; Tasis, D.; Papagelis, K.; Galiotis, C. Carbon nanotube-polymer composites: Chemistry, processing, mechanical, and electrical properties. *Prog. Polym. Sci.* **2010**, *35*, 357–401.
[92] Collins, P. G.; Avouris, P. The electronic properties of carbon nanotubes. *Contemp. Concep. Conden. Matt. Sci.*, **2008**, *3*, 49–81.
[93] Flygare, M.; Svensson, K. Influence of crystallinity on the electrical conductivity of individual carbon nanotubes. *Carbon Trends.* **2021**, *5*, 100125.
[94] Collins, P. G.; Arnold, M. S.; Avouris, P. Engineering carbon nanotubes and nanotube circuits using electrical breakdown. *Science* **2001**, *292*, 706–709.
[95] Das, S. A review on Carbon Nano-tubes—A new era of nanotechnology. *Int. J. Emerg. Technol. Adv. Eng.* **2013**, *3*, 774–783.
[96] Treacy, M. M. J.; Ebbesen, T. W.; Gibson, J. M. Exceptionally high Young's modulus observed for individual carbon nanotubes. *Nature* **1996**, *381*, 678–680.
[97] Goudah, G.; Suliman, S. M. A.; Elfaki, E. A. Carbon nanotubes: Challenges and opportunities. In *2013 International Conference on Computing, Electrical, and Electronic Engineering* (*ICCEEE*), Khartoum, Sudan, 2013, pp 74–81.
[98] Abdalla, M.; Dean, D.; Theodore, M.; Fielding, J.; Nyairo, E.; Price, G. Magnetically processed carbon nanotube/epoxy nanocomposites: Morphology, thermal, and mechanical properties. *Polymer* **2010**, *51*, 1614–1620.

[99] Lan, Y. C.; Wang, Y.; Ren, Z. F. Physics and applications of aligned carbon nanotubes. *Adv. Phys.* **2011**, *60*, 553–678.
[100] Yu, M. F.; Files, B. S.; Arepalli, S.; Ruoff, R. S. Tensile loading of ropes of single wall carbon nanotubes and their mechanical properties. *Phys. Rev. Lett.* **2000**, *84*, 5552–5555.
[101] Ruoff, R. S.; Tersoff, J.; Lorents, D. C.; Subramoney, S.; Chan, B. Radial deformation of carbon nanotubes by van der Waals forces. *Nature* **1993**, *364*, 514–516.
[102] Pothnis, J. R.; Kalyanasundaram, D.; Gururaja, S. Enhancement of open hole tensile strength via alignment of carbon nanotubes infused in glass fiber-epoxy-CNT multi-scale composites. *Compos. Part A: Appl. Sci. Manuf.* **2021**, *140*, 106155.
[103] Chen, S.; Tao, K. J.; Chen, X.; Meng, Y. Q.; Wang, M. Y.; Zhou, J.; Chen, C.; Wang, Y. L.; Hui, K. N.; Bielawski, C. W. et al. Regulating lithium plating and stripping by using vertically aligned graphene/CNT channels decorated with ZnO particles. *Chem.—Eur. J.* **2021**, *27*, 15706–15715.
[104] Sun, X. M.; Chen, T.; Yang, Z. B.; Peng, H. S. The alignment of carbon nanotubes: An effective route to extend their excellent properties to macroscopic scale. *Acc. Chem. Res.* **2013**, *46*, 539–549.
[105] Zhang, H.; Cao, G. P.; Yang, Y. S.; Gu, Z. N. Comparison between electrochemical properties of aligned carbon nanotube array and entangled carbon nanotube electrodes. *J. Electrochem. Soc.* **2008**, *155*, K19–K22.
[106] Rahman, R.; Servati, P. Effects of inter-tube distance and alignment on tunnelling resistance and strain sensitivity of nanotube/polymer composite films. *Nanotechnology* **2012**, *23*, 055703.
[107] Thostenson, E. T.; Chou, T. W. Aligned multi-walled carbon nanotube-reinforced composites: Processing and mechanical characterization. *J. Phys. D Appl. Phys.* **2002**, *35*, L77–L80.
[108] Mei, H.; Bai, Q. L.; Dassios, K.; Li, H. Q.; Cheng, L. F.; Galiotis, C. Morphological and microstructural property comparison of bulk and aligned Cvd-grown carbon nanotubes. *Adv. Compos. Lett.* **2014**, *23*, 10.1177/096369351402300101.
[109] Chen, J. J. Effects of structure, purity, and alignment on the heat conduction properties of a nanostructured material comprising carbon nanotubes. *DYSONA Appl. Sci.* **2022**, *3*, 46–55.
[110] Cao, Q.; Hur, S. H.; Zhu, Z. T.; Sun, Y. G.; Wang, C. J.; Meitl, M. A.; Shim, M.; Rogers, J. A. Highly bendable, transparent thin-film transistors that use carbon-nanotube-based conductors and semiconductors with elastomeric dielectrics. *Adv. Mater.* **2006**, *18*, 304–309.
[111] Ishikawa, F. N.; Chang, H. K.; Ryu, K.; Chen, P. C.; Badmaev, A.; De Arco, L. G.; Shen, G. Z.; Zhou, C. W. Transparent electronics based on transfer printed aligned carbon nanotubes on rigid and flexible substrates. *ACS Nano* **2009**, *3*, 73–79.
[112] Seah, C. M.; Chai, S. P.; Mohamed, A. R. Synthesis of aligned carbon nanotubes. *Carbon* **2011**, *49*, 4613–4635.
[113] Zhang, M.; Atkinson, K. R.; Baughman, R. H. Multifunctional carbon nanotube yarns by downsizing an ancient technology. *Science* **2004**, *306*, 1358–1361.
[114] Liu, K.; Sun, Y. H.; Chen, L.; Feng, C.; Feng, X. F.; Jiang, K. L.; Zhao, Y. G.; Fan, S. S. Controlled growth of super-aligned carbon nanotube arrays for spinning continuous unidirectional sheets with tunable physical properties. *Nano Lett.* **2008**, *8*, 700–705.
[115] Goh, P. S.; Ismail, A. F.; Ng, B. C. Directional alignment of carbon nanotubes in polymer matrices: Contemporary approaches and future advances. *Compos. Part A: Appl. Sci. Manuf.* **2014**, *56*, 103–126.
[116] Goh, G. L.; Agarwala, S.; Yeong, W. Y. Directed and on-demand alignment of carbon nanotube: A review toward 3D printing of electronics. *Adv. Mater. Interfaces* **2019**, *6*, 1801318.
[117] Ma, Y. F.; Wang, B.; Wu, Y. P.; Huang, Y.; Chen, Y. S. The production of horizontally aligned single-walled carbon nanotubes. *Carbon* **2011**, *49*, 4098–4110.
[118] Azam, M. A.; Manaf, N. S. A.; Talib, E.; Bistamam, M. S. A. Aligned carbon nanotube from catalytic chemical vapor deposition technique for energy storage device: A review. *Ionics* **2013**, *19*, 1455–1476.
[119] Zhang, R. F.; Zhang, Y. Y.; Wei, F. Horizontally aligned carbon nanotube arrays: Growth mechanism, controlled synthesis, characterization, properties, and applications. *Chem. Soc. Rev.* **2017**, *46*, 3661–3715.
[120] Yin, Z. F.; Ding, A.; Zhang, H.; Zhang, W. The relevant approaches for aligning carbon nanotubes. *Micromachines (Basel)* **2022**, *13*, 1863.
[121] Cao, Y. F.; Zhou, T.; Wu, K. J.; Yong, Z. Z.; Zhang, Y. Y. Aligned carbon nanotube fibers for fiber-shaped solar cells, supercapacitors, and batteries. *RSC Adv.* **2021**, *11*, 6628–6643.
[122] Kohls, A.; Ditty, M. M.; Dehghandehnavi, F.; Zheng, S. Y. Vertically aligned carbon nanotubes as a unique material for biomedical applications. *ACS Appl. Mater. Interfaces* **2022**, *14*, 6287–6306.
[123] Mizuno, K.; Ishii, J.; Kishida, H.; Hayamizu, Y.; Yasuda, S.; Futaba, D. N.; Yumura, M.; Hata, K. A black body absorber from vertically aligned single-walled carbon nanotubes. *Proc. Natl. Acad. Sci. USA* **2009**, *106*, 6044–6047.
[124] Paul, S. J.; Elizabeth, I.; Gupta, B. K. Ultrasensitive wearable strain sensors based on a VACNT/PDMS thin film for a wide range of human motion monitoring. *ACS Appl. Mater. Interfaces* **2021**, *13*, 8871–8879.
[125] Ertl, G. Press Release, Nobel Prize, Chemie 2019. *Nobel Lect. Chem.* **2015**, 37–69.
[126] Winter, M.; Barnett, B.; Xu, K. Before Li Ion batteries. *Chem. Rev.* **2018**, *118*, 11433–11456.
[127] Mezei, F. 2011. Basics concepts. In *Neutrons in Soft Matter*; Imae, T.; Kanaya, T.; Furusaka, M.; Torikai, N., Eds.; John Wiley & Sons, Inc.: Hoboken, 2011; pp 1–28.
[128] Doeff, M. M. Batteries: Overview of Battery Cathodes. Lawrence Berkeley National Laboratory: Berkeley., 2014: 709–739.
[129] Goodenough, J. B.; Park, K. S. The Li-ion rechargeable battery: A perspective. *J. Am. Chem. Soc.* **2013**, *135*, 1167–1176.
[130] De Las Casas, C.; Li, W. Z. A review of application of carbon nanotubes for lithium ion battery anode material. *J. Power Sources* **2012**, *208*, 74–85.
[131] Lee, S. H.; Yu, S. H.; Lee, J. E.; Jin, A. H.; Lee, D. J.; Lee, N.; Jo, H.; Shin, K.; Ahn, T. Y.; Kim, Y. W. et al. Self-assembled Fe_3O_4 nanoparticle clusters as high-performance anodes for lithium ion batteries via geometric confinement. *Nano Lett.* **2013**, *13*, 4249–4256.
[132] Wang, H. L.; Cui, L. F.; Yang, Y.; Casalongue, H. S.; Robinson, J. T.; Liang, Y. Y.; Cui, Y.; Dai, H. J. Mn_3O_4-graphene hybrid as a high-capacity anode material for lithium ion batteries. *J. Am. Chem. Soc.* **2010**, *132*, 13978–13980.a.
[133] Cabana, J.; Monconduit, L.; Larcher, D.; Palacín, M. R. Beyond intercalation-based Li-ion batteries: The state of the art and challenges of electrode materials reacting through conversion reactions. *Adv. Mater.* **2010**, *22*, E170–E192.
[134] Su, J.; Gao, Z. G.; Xie, Y. Y.; Zhang, Z. L.; Wang, H. Boosting Li-storage properties of conversion-type anodes for lithium-ion batteries via steric effect of intercalation-type materials: A case of $MnCO_3$. *Compos. Part B: Eng.* **2021**, *212*, 108733.
[135] Lee, S.; Song, M.; Kim, S.; Mathew, V.; Sambandam, B.; Hwang, J. Y.; Kim, J. High lithium storage properties in a manganese sulfide anodeviaan intercalation-cum-conversion reaction. *J. Mater. Chem. A* **2020**, *8*, 17537–17549.
[136] Tagbo, P. C.; Okaro, C. A.; Ugwuoke, C. O.; Obetta, H. U.; Okwundu, O. S.; Ezugwu, S.; Ezema, F. I. Zinc anode in hydrodynamically enhanced aqueous battery systems. In *Electrode Materials for Energy Storage and Conversion*; Kebede, M. A.; Ezema, F. I. , Eds.; CRC Press: Boca Raton, 2021; pp 47–70.
[137] Yu, S. H.; Feng, X. R.; Zhang, N.; Seok, J.; Abruña, H. D. Understanding conversion-type electrodes for lithium rechargeable batteries. *Acc. Chem. Res.* **2018**, *51*, 273–281.
[138] Wang, F.; Robert, R.; Chernova, N. A.; Pereira, N.; Omenya, F.; Badway, F.; Hua, X.; Ruotolo, M.; Zhang, R. G.; Wu, L. J. et al. Conversion reaction mechanisms in lithium ion batteries: Study of the binary metal fluoride electrodes. *J. Am. Chem. Soc.* **2011**, *133*, 18828–18836.
[139] Sun, Y. M.; Liu, N.; Cui, Y. Promises and challenges of nanomaterials for lithium-based rechargeable batteries. *Nat. Energy*

2016, *1*, 16071.
[140] Goward, G. R.; Taylor, N. J.; Souza, D. C. S.; Nazar, L. F. The true crystal structure of $Li_{17}M_4$ (M = Ge, Sn, Pb)-revised from $Li2_2M_5$. *J. Alloys Compd.* **2001**, *329*, 82–91.
[141] Garcia, A.; Biswas, S.; McNulty, D.; Roy, A.; Raha, S.; Trabesinger, S.; Nicolosi, V.; Singha, A.; Holmes, J. D. One-step grown carbonaceous germanium nanowires and their application as highly efficient lithium-ion battery anodes. *ACS Appl. Energy Mater.* **2022**, *5*, 1922–1932.
[142] Chan, C. K.; Patel, R. N.; O'Connell, M. J.; Korgel, B. A.; Cui, Y. Solution-grown silicon nanowires for lithium-ion battery anodes. *ACS Nano* **2010**, *4*, 1443–1450.
[143] Wang, F.; Li, P.; Li, W.; Wang, D. H. Electrochemical synthesis of multidimensional nanostructured silicon as a negative electrode material for lithium-ion battery. *ACS Nano* **2022**, *16*, 4689–7700.
[144] Gavrilin, I. M.; Kudryashova, Y. O.; Kuz'mina, A. A.; Kulova, T. L.; Skundin, A. M.; Emets, V. V.; Volkov, R. L.; Dronov, A. A.; Borgardt, N. I.; Gavrilov, S. A. High-rate and low-temperature performance of germanium nanowires anode for lithium-ion batteries. *J. Electroanal. Chem.* **2021**, *888*, 115209.
[145] Yang, Z. X.; Dong, Y. J.; Liu, C.; Feng, X. Q.; Jin, H. C.; Ma, X. H.; Ding, F.; Li, B. Q.; Bai, L. Y.; Ouyang, Y. G. et al. Design and synthesis of high-silicon silicon suboxide nanowires by radio-frequency thermal plasma for high-performance lithium-ion battery anodes. *Appl. Surf. Sci.* **2023**, *614*, 156235.
[146] Gao, S. S.; Zhao, T. Y.; Wang, D. X.; Huang, J.; Xiang, Y. L.; Yu, Y. J. Ge nanowires on top of a Ge substrate for applications in anodes of Li and Na ion batteries: A first-principles study. *RSC Adv.* **2022**, *12*, 9163–9169.
[147] Chandran, K. S. R. A critical review of silicon nanowire electrodes and their energy storage capacities in Li-ion cells. *RSC Adv.* **2023**, *13*, 3947–3957.
[148] Zheng, X.; Miao, X.; Xiao, Y. F.; Chen, Y.; Hu, T.; Gong, X. H.; Wu, C. G.; Wang, G. J.; Hou, Y. J. Synthesis and electrochemical performance of Ag nanowires coating tungsten diselenide as efficient nanocomposite for lithium-ion storage. *Mater. Lett.* **2023**, *336*, 133820.
[149] Rashad, M.; Geaney, H. Vapor-solid-solid growth of silicon nanowires using magnesium seeds and their electrochemical performance in Li-ion battery anodes. *Chem. Eng. J.* **2023**, *452*, 139397.
[150] Wen, Z. H.; Lu, G. H.; Mao, S.; Kim, H.; Cui, S. M.; Yu, K. H.; Huang, X. K.; Hurley, P. T.; Mao, O.; Chen, J. H. Silicon nanotube anode for lithium-ion batteries. *Electrochem. Commun.* **2013**, *9*, 67–70.
[151] Song, T.; Xia, J. L.; Lee, J. H.; Lee, D. H.; Kwon, M. S.; Choi, J. M.; Wu, J.; Doo, S. K.; Chang, H.; Park, W. I. et al. Arrays of sealed silicon nanotubes as anodes for lithium ion batteries. *Nano Lett.* **2010**, *10*, 1710–1716.
[152] Guo, T.; Luo, G. Y.; Shi, C. Y.; Shi, H. L.; Shi, Z. X.; He, B. F.; Chen, J. B. Thermal burst synthesis of high-performance Si nanotube sheets for lithium-ion batteries. *ACS Sustainable Chem. Eng.* **2022**, *10*, 4031–4039.
[153] Kim, J. H.; Kim, S.; Han, J. H.; Seo, S. B.; Choi, Y. R.; Lim, J.; Kim, Y. A. Perspective on carbon nanotubes as conducting agent in lithium-ion batteries: The status and future challenges. *Carbon Lett.* **2023**, *33*, 325–333.
[154] Yang, X. X.; Wu, L. W.; Hou, J.; Meng, B. Y.; Ali, R.; Liu, Y. F.; Jian, X. Symmetrical growth of carbon nanotube arrays on FeSiAl micro-flake for enhancement of lithium-ion battery capacity. *Carbon* **2022**, *189*, 93–103.
[155] Zhong, S. Y.; Liu, H. Z.; Wei, D. H.; Hu, J.; Zhang, H.; Hou, H. S.; Peng, M. X.; Zhang, G. H.; Duan, H. G. Long-aspect-ratio N-rich carbon nanotubes as anode material for sodium and lithium ion batteries. *Chem. Eng. J.* **2020**, *395*, 125054.
[156] Moyer-Vanderburgh, K.; Ma, M. C.; Park, S. J.; Jue, M. L.; Buchsbaum, S. F.; Wu, K. J.; Wood, M.; Ye, J. C.; Fornasiero, F. Growth and performance of high-quality SWCNT forests on Inconel foils as lithium-ion battery anodes. *ACS Appl. Mater. Interfaces* **2022**, *14*, 54981–54991.
[157] Chen, H. Y.; Li, M. X.; Li, C. P.; Li, X.; Wu, Y. L.; Chen, X. C.; Wu, J. X.; Li, X. Y.; Chen, Y. M. Electrospun carbon nanofibers for lithium metal anodes: Progress and perspectives. *Chin. Chem. Lett.* **2022**, *33*, 141–152.
[158] Zhao, Y.; Yan, J. H.; Yu, J. Y.; Ding, B. Electrospun nanofiber electrodes for lithium-ion batteries. *Macromol. Rapid Commun.* **2022**, *44*, 2200740.
[159] Xin, Y.; Mou, H. Y.; Miao, C.; Nie, S. Q.; Wen, M. Y.; He, G. W.; Xiao, W. Encapsulating Sn-Cu alloy particles into carbon nanofibers as improved performance anodes for lithium-ion batteries. *J. Alloys Compd.* **2022**, *922*, 166176.
[160] Culebras, M.; Collins, G. A.; Beaucamp, A.; Geaney, H.; Collins, M. N. Lignin/Si hybrid carbon nanofibers towards highly efficient sustainable Li-ion anode materials. *Eng. Sci.* **2022**, *17*, 195–203.
[161] Jiao, L. S.; Liu, Z. B.; Sun, Z. H.; Wu, T. S.; Gao, Y. Z.; Li, H. Y.; Li, F. H.; Niu, L. An advanced lithium ion battery based on a high quality graphitic graphene anode and a $Li[Ni_{0.6}Co_{0.2}Mn_{0.2}]O_2$ cathode. *Electrochim. Acta* **2018**, *259*, 48–55.
[162] Kukułka, W.; Kierzek, K.; Stankiewicz, N.; Chen, X. C.; Tang, T.; Mijowska, E. Well-designed porous graphene flakes for lithium-ion batteries with outstanding rate performance. *Langmuir* **2019**, *35*, 12613–12619.
[163] Kumar, R.; Sahoo, S.; Joanni, E.; Singh, R. K.; Tan, W. K.; Kar, K. K.; Matsuda, A. Recent progress in the synthesis of graphene and derived materials for next generation electrodes of high performance lithium ion batteries. *Prog. Energy Combust. Sci.* **2019**, *75*, 100786.
[164] Sun, H.; Varzi, A.; Pellegrini, V.; Dinh, D. A.; Raccichini, R.; Del Rio-Castillo, A. E.; Prato, M.; Colombo, M.; Cingolani, R.; Scrosati, B. et al. How much does size really matter. Exploring the limits of graphene as Li ion battery anode material. *Solid State Commun.* **2017**, *251*, 88–93.
[165] Kokai, F.; Sorin, R.; Chigusa, H.; Hanai, K.; Koshio, A.; Ishihara, M.; Koga, Y.; Hasegawa, M.; Imanishi, N.; Takeda, Y. Ultrasonication fabrication of high quality multilayer graphene flakes and their characterization as anodes for lithium ion batteries. *Diam. Relat. Mater.* **2012**, *29*, 63–68.
[166] Kim, W. S.; Hwa, Y.; Jeun, J. H.; Sohn, H. J.; Hong, S. H. Synthesis of SnO_2 Nano hollow spheres and their size effects in lithium ion battery anode application. *J. Power Sources* **2013**, *225*, 108–112.
[167] Wang, F.; Wang, B.; Yu, Z. L.; Lv, Q.; Jin, F.; Bao, C. Y.; Wang, D. L. A simple and green self-conversion method to construct silicon hollow spheres for high-performance Li-ion battery anodes. *Electrochim. Acta* **2023**, *443*, 141950.
[168] Pan, Q. C.; Ding, Y. J.; Yan, Z. X.; Cai, Y. Z.; Zheng, F. H.; Huang, Y. G.; Wang, H. Q.; Li, Q. Y. Designed synthesis of Fe_3O_4@NC yolk–shell hollow spheres as high performance anode material for lithium-ion batteries. *J. Alloys Compd.* **2020**, *821*, 153569.
[169] Sun, B.; Chen, Z. X.; Kim, H. S.; Ahn, H.; Wang, G. X. MnO/C core–shell nanorods as high capacity anode materials for lithium-ion batteries. *J. Power Sources* **2011**, *196*, 3346–3349.
[170] Van, C. D.; Jeong, J. R.; Yoon, K.; Kang, K.; Lee, M. H. Core–shell structure of Mo-based nanoparticle/carbon nanotube/amorphous carbon composites as high-performance anodes for lithium-ion batteries. *ACS Appl. Nano Mater.* **2022**, *5*, 6555–6563.
[171] Su, J. T.; Lin, S. H.; Cheng, C. C.; Cheng, P. Y.; Lu, S. Y. Porous core–shell B-doped silicon-carbon composites as electrode materials for lithium ion capacitors. *J. Power Sources* **2022**, *531*, 231345.
[172] An, W. L.; He, P.; Che, Z. Z.; Xiao, C. M.; Guo, E. M.; Pang, C. L.; He, X. Q.; Ren, J. G.; Yuan, G. H.; Du, N. et al. Scalable synthesis of pore-rich Si/C@C core–shell-structured microspheres for practical long-life lithium-ion battery anodes. *ACS Appl. Mater. Interfaces* **2022**, *14*, 10308–10318.
[173] Sun, C. H.; Lin, Y. Y.; Li, W. L.; Fan, Y. C.; Liu, H. Y.; Sun, Y. H.; Nan, J. M. *In-situ* growth of core–shell structure of tremella fuciformis shaped SnS@Sulfur doped carbon composite as anode materials for high performance lithium-ion batteries. *J. Alloys Compd.* **2023**, *935*, 168087.

[174] Shi, Q. T.; Zhou, J. H.; Ullah, S.; Yang, X. Q.; Tokarska, K.; Trzebicka, B.; Ta, H. Q.; Rümmeli, M. H. A review of recent developments in Si/C composite materials for Li-ion batteries. *Energy Storage Mater.* **2021**, *34*, 735–754.
[175] Yang, X.; Zheng, G. X.; Wang, Q. Y.; Chen, X.; Han, Y.; Zhang, D. Q.; Zhang, Y. C. Functional application of multi-element metal composite materials. *J. Alloys Compd.* **2022**, *895*, 162622.
[176] Rehman, W. U.; Jiang, Z. Y.; Qu, Z. G.; Xu, Y. L.; Wang, X.; Ullah, I. Preparation of Mn_2SnO_4 wrapped with N-doped reduced graphene oxide as a stable anode material for lithium-ion storage. *J. Alloys Compd.* **2023**, *939*, 168829.
[177] Yuan, S.; Lai, Q. H.; Duan, X.; Wang, Q. Carbon-based materials as anode materials for lithium-ion batteries and lithium-ion capacitors: A review. *J. Energy Storage* **2023**, *61*, 106716.
[178] Wang, Y.; Luo, S. N.; Chen, M.; Wu, L. M. Uniformly confined germanium quantum dots in 3D ordered porous carbon framework for high-performance Li-ion battery. *Adv. Funct. Mater.* **2020**, *30*, 2000373.
[179] Wei, C. L.; Wang, Y. S.; Zhang, Y. C.; Tan, L. W.; Qian, Y.; Tao, Y.; Xiong, S. L.; Feng, J. K. Flexible and stable 3D lithium metal anodes based on self-standing MXene/COF frameworks for high-performance lithium-sulfur batteries. *Nano Res.* **2021**, *14*, 3576–3584.
[180] Gao, W. L.; Pumera, M. 3D printed nanocarbon frameworks for Li-ion battery cathodes. *Adv. Funct. Mater.* **2021**, *31*, 2007285.
[181] Li, Y. J.; Li, J. P.; Xiao, H.; Xie, T. C.; Zheng, W. T.; He, J. L.; Zhu, H. J.; Huang, S. M. A novel 3D Li/Li_9Al_4/Li-Mg alloy anode for superior lithium metal batteries. *Adv. Funct. Mater.* **2023**, *33*, 2213905.
[182] Chen, Y.; Zou, Y. M.; Shen, X. P.; Qiu, J. X.; Lian, J. B.; Pu, J. R.; Li, S.; Du, F. H.; Li, S. Q.; Ji, Z. Y. et al. Ge nanoparticles uniformly immobilized on 3D interconnected porous graphene frameworks as anodes for high-performance lithium-ion batteries. *J. Energy Chem.* **2022**, *69*, 161–173.
[183] Burukhin, A.; Brylev, O.; Hany, P.; Churagulov, B. R. Hydrothermal synthesis of LiCoO2 for lithium rechargeable batteries. *Solid State Ion.* **2002**, *151*, 259–263.
[184] Cao, Q.; Zhang, H. P.; Wang, G. J.; Xia, Q.; Wu, Y. P.; Wu, H. Q. A novel carbon-coated $LiCoO_2$ as cathode material for lithium ion battery. *Electrochem. Commun.* **2007**, *9*, 1228–1232.
[185] Zhang, J.; Xiang, Y. J.; Yu, Y.; Xie, S.; Jiang, G. S.; Chen, C. H. Electrochemical evaluation and modification of commercial lithium cobalt oxide powders. *J. Power Sources* **2004**, *132*, 187–194.
[186] Huang, X.; Rui, X. H.; Hng, H. H.; Yan, Q. Y. Vanadium pentoxide-based cathode materials for lithium-ion batteries: Morphology control, carbon hybridization, and cation doping. *Part. Part. Syst. Charact.* **2015**, *32*, 276–294.
[187] Tang, X.; Lin, B. H.; Ge, Y.; Ge, Y.; Lu, C. J.; Savilov, S. V.; Aldoshin, S. M.; Xia, H. $LiMn_2O_4$ nanorod arrays: A potential three-dimensional cathode for lithium-ion microbatteries. *Mater. Res. Bull.* **2015**, *69*, 2–6.
[188] Gnanaraj, J. S.; Pol, V. G.; Gedanken, A.; Aurbach, D. Improving the high-temperature performance of $LiMn_2O_4$ spinel electrodes by coating the active mass with MgO via a sonochemical method. *Electrochem. Commun.* **2003**, *5*, 940–945.
[189] Eftekhari, A. $LiMn_2O_4$ electrode prepared by gold-titanium codeposition with improved cyclability. *J. Power Sources* **2004**, *130*, 260–265.
[190] Xu, Y. N.; Chung, S. Y.; Bloking, J. T.; Chiang, Y. M.; Ching, W. Y. Electronic structure and electrical conductivity of undoped $LiFePO_4$. *Electrochem. Solid-State Lett.* **2004**, *7*, A131–A134.
[191] Shi, S. Q.; Liu, L. J.; Ouyang, C. Y.; Wang, D. S.; Wang, Z. X.; Chen, L. Q.; Huang, X. J. Enhancement of electronic conductivity of $LiFePO_4$ by Cr doping and its identification by first-principles calculations. *Phys. Rev. B* **2003**, *68*, 195108.
[192] Prosini, P. P.; Lisi, M.; Zane, D.; Pasquali, M. Determination of the chemical diffusion coefficient of lithium in $LiFePO_4$. *Solid State Ion.* **2002**, *148*, 45–51.
[193] Kang, J.; Mathew, V.; Gim, J.; Kim, S.; Song, J. J.; Im, W. B.; Han, J.; Lee, J. Y.; Kim, J. Pyro-synthesis of a high rate nano-$Li_3V_2(PO_4)_3$/C cathode with mixed morphology for advanced Li-ion batteries. *Sci. Rep.* **2015**, *4*, 4047.
[194] Wang, Q. H.; Xu, J. T.; Zhang, W. C.; Mao, M. L.; Wei, Z. X.; Wang, L.; Cui, C. Y.; Zhu, Y. X.; Ma, J. M. Research progress on vanadium-based cathode materials for sodium ion batteries. *J. Mater. Chem. A* **2018**, *6*, 8815–8838.
[195] Wang, Y.; Cao, G. Z. Developments in nanostructured cathode materials for high-performance lithium-ion batteries. *Adv. Mater.* **2008**, *20*, 2251–2269.
[196] Wang, S. Q.; Lu, Z. D.; Wang, D.; Li, C. G.; Chen, C. H.; Yin, Y. D. Porous monodisperse V_2O_5 microspheres as cathode materials for lithium-ion batteries. *J. Mater. Chem.* **2011**, *21*, 6365–6369.
[197] Mai, L.; Xu, L.; Han, C. H.; Xu, X.; Luo, Y. Z.; Zhao, S. Y.; Zhao, Y. L. Electrospun ultralong hierarchical vanadium oxide nanowires with high performance for lithium ion batteries. *Nano Lett.* **2010**, *10*, 4750–4755.
[198] Ventrapragada, L. K.; Zhu, J. Y.; Creager, S. E.; Rao, A. M.; Podila, R. A versatile carbon nanotube-based scalable approach for improving interfaces in Li-ion battery electrodes. *ACS Omega.* **2018**, *3*, 4502–4508.
[199] Cao, W. J.; Greenleaf, M.; Li, Y. X.; Adams, D.; Hagen, M.; Doung, T.; Zheng, J. P. The effect of lithium loadings on anode to the voltage drop during charge and discharge of Li-ion capacitors. *J. Power Sources* **2015**, *280*, 600–605.
[200] Luo, Y. F.; Wang, K.; Li, Q. Q.; Fan, S. S.; Wang, J. P. Macroscopic carbon nanotube structures for lithium batteries. *Small* **2020**, *16*, 1902719.
[201] Lu, W.; Goering, A.; Qu, L. T.; Dai, L. M. Lithium-ion batteries based on vertically-aligned carbon nanotube electrodes and ionic liquid electrolytes. *Phys. Chem. Chem. Phys.* **2012**, *14*, 12099–12104.
[202] Yang, Z. H.; Wu, H. Q. Electrochemical intercalation of lithium into raw carbon nanotubes. *Mater. Chem. Phys.* **2001**, *71*, 7–11.
[203] Zhao, J. J.; Buldum, A.; Han, J.; Lu, J. P. First-principles study of Li-intercalated carbon nanotube ropes. *Phys. Rev. Lett.* **2000**, *85*, 1706–1709.
[204] Nishidate, K.; Hasegawa, M. Energetics of lithium ion adsorption on defective carbon nanotubes. *Phys. Rev. B* **2005**, *71*, 245418.
[205] Nishidate, K.; Sasaki, K.; Oikawa, Y.; Baba, M.; Hasegawa, M. Density functional electronic structure calculations of lithium ion adsorption on defective carbon nanotubes. *e-J. l Surf. Sci. Nanotechnol.* **2005**, *3*, 358–361.
[206] Fagan, S. B.; Guerini, S.; Filho, J. M.; Lemos, V. Lithium intercalation into single-wall carbon nanotube bundles. *Microelectron. J.* **2005**, *36*, 499–501.
[207] Senami, M.; Ikeda, Y.; Fukushima, A.; Tachibana, A. Theoretical study of adsorption of lithium atom on carbon nanotube. *AIP Adv.* **2011**, *1*, 042106.
[208] Shimoda, H.; Gao, B.; Tang, X. P.; Kleinhammes, A.; Fleming, L.; Wu, Y.; Zhou, O. Lithium intercalation into opened single-wall carbon nanotubes: Storage capacity and electronic properties. *Phys. Rev. Lett.* **2002**, *88*, 015502.
[209] Khantha, M.; Cordero, N. A.; Alonso, J. A.; Cawkwell, M.; Girifalco, L. A. Interaction and concerted diffusion of lithium in a (5, 5) carbon nanotube. *Phys. Rev. B* **2008**, *78*, 115430.
[210] Yang, J. L.; Liu, H. J.; Chan, C. T. Theoretical study of alkali-atom insertion into small-radius carbon nanotubes to form single-atom chains. *Phys. Rev. B* **2001**, *64*, 085420.
[211] Zhao, M. W.; Xia, Y. Y.; Liu, X. D.; Tan, Z. Y.; Huang, B. D.; Li, F.; Ji, Y. J.; Song, C. Curvature-induced condensation of lithium confined inside single-walled carbon nanotubes: First-principles calculations. *Phys. Lett. A* **2005**, *340*, 434–439.
[212] Meunier, V.; Kephart, J.; Roland, C.; Bernholc, J. *Ab initio* investigations of lithium diffusion in carbon nanotube systems. Phys. Rev. *Lett.* **2002**, *88*, 075506.
[213] Dubot, P.; Cenedese, P. Modeling of molecular hydrogen and lithium adsorption on single-wall carbon nanotubes. *Phys. Rev. B* **2001**, *63*, 241402.
[214] Garau, C.; Frontera, A.; Quiñonero, D.; Costa, A.; Ballester, P.; Deyà, P. M. *Ab initio* investigations of lithium diffusion in single-walled carbon nanotubes. *Chem. Phys.* **2004**, *297*, 85–91.
[215] Yang, S. B.; Huo, J. P.; Song, H. H.; Chen, X. H. A comparative

study of electrochemical properties of two kinds of carbon nanotubes as anode materials for lithium ion batteries. *Electrochim. Acta.* **2008**, *53*, 2238–2244.
[216] Gao, B.; Bower, C.; Lorentzen, J. D.; Fleming, L.; Kleinhammes, A.; Tang, X. P.; McNeil, L. E.; Wu, Y.; Zhou, O. Enhanced saturation lithium composition in ball-milled single-walled carbon nanotubes. *Chem. Phys. Lett.* **2000**, *327*, 69–75.
[217] Mi, C. H.; Cao, G. S.; Zhao, X. B. A non-GIC mechanism of lithium storage in chemical etched MWNTs. *J. Electroanal. Chem.* **2004**, *562*, 217–221.
[218] Garau, C.; Frontera, A.; Quiñonero, D.; Costa, A.; Ballester, P.; Deyà, P. M. Lithium diffusion in single-walled carbon nanotubes: A theoretical study. *Chem. Phys. Lett.* **2003**, *374*, 548–555.
[219] Frackowiak, E.; Béguin, F. Electrochemical storage of energy in carbon nanotubes and nanostructured carbons. *Carbon* **2002**, *40*, 1775–1787.
[220] Hresko, W. Feature article. *Remedial Spec. Educ.* **1989**, *10*, 8.
[221] Eatemadi, A.; Daraee, H.; Karimkhanloo, H.; Kouhi, M.; Zarghami, N.; Akbarzadeh, A.; Abasi, M.; Hanifehpour, Y.; Joo, S. W. Carbon nanotubes: Properties, synthesis, purification, and medical applications. *Nanoscale Res. Lett.* **2014**, *9*, 393.
[222] Thess, A.; Lee, R.; Nikolaev, P.; Dai, H. J.; Petit, P.; Robert, J.; Xu, C. H.; Lee, Y. H.; Kim, S. G.; Rinzler, A. G. et al. Crystalline ropes of metallic carbon nanotubes. *Science* **1996**, *273*, 483–487.
[223] Kawasaki, S.; Hara, T.; Iwai, Y.; Suzuki, Y. Metallic and semiconducting single-walled carbon nanotubes as the anode material of Li ion secondary battery. *Mater. Lett.* **2008**, *62*, 2917–2920.
[224] Reddy, A. L. M.; Shaijumon, M. M.; Gowda, S. R.; Ajayan, P. M. Coaxial MnO_2/carbon nanotube array electrodes for high-performance lithium batteries. *Nano Lett.* **2009**, *9*, 1002–1006.
[225] Zhang, H. X.; Feng, C.; Zhai, Y. C.; Jiang, K. L.; Li, Q. Q.; Fan, S. S. Cross-stacked carbon nanotube sheets uniformly loaded with SnO_2 nanoparticles: A novel binder-free and high-capacity anode material for lithium-ion batteries. *Adv. Mater.* **2009**, *21*, 2299–2304.
[226] Chen, N. N.; Chen, L.; Li, W. X.; Xu, Z. W.; Qian, X. M.; Liu, Y. Brush-like Ni/carbon nanofibers/carbon nanotubes multi-layer network for freestanding anode in lithium ion batteries. *Ceram. Int.* **2019**, *45*, 16676–16681.
[227] Zhang, H.; Cao, G. P.; Wang, Z. Y.; Yang, Y. S.; Shi, Z. J.; Gu, Z. N. Carbon nanotube array anodes for high-rate Li-ion batteries. *Electrochim. Acta* **2010**, *55*, 2873–2877.
[228] Man, Y. H.; Zhang, Y. P.; Guo, P. T. Freestanding ultralong aligned carbon nanotube films as electrode materials for a lithium-ion battery. *Adv. Mater. Res.* **2013**, *798–799*, 143–146.
[229] Bulusheva, L. G.; Arkhipov, V. E.; Fedorovskaya, E. O.; Zhang, S.; Kurenya, A. G.; Kanygin, M. A.; Asanov, I. P.; Tsygankova, A. R.; Chen, X. H.; Song, H. H. et al. Fabrication of free-standing aligned multiwalled carbon nanotube array for Li-ion batteries. *J. Power Sources* **2016**, *311*, 42–48.
[230] Masarapu, C.; Subramanian, V.; Zhu, H. W.; Wei, B. Q. Long-cycle electrochemical behavior of multiwall carbon nanotubes synthesized on stainless steel in Li ion batteries. *Adv. Funct. Mater.* **2009**, *19*, 1008–1014.
[231] Wang, G. X.; Yao, J.; Liu, H. K.; Dou, S. X.; Ahn, J. H. Growth and lithium storage properties of vertically aligned carbon nanotubes. *Met. Mater. Int.* **2006**, *12*, 413–416.
[232] Jung, H. Y.; Hong, S.; Yu, A.; Jung, S. M.; Jeoung, S. K.; Jung, Y. J. Efficient lithium storage from modified vertically aligned carbon nanotubes with open-ends. *RSC Adv.* **2015**, *5*, 68875–68880.
[233] Ghosh, M.; Venkatesh, G.; Rao, G. M. Vertically aligned and tree-like carbon nanostructures as anode of lithium ion battery. *Diam. Relat. Mater.* **2018**, *87*, 56–60.
[234] Wang, X. H.; Sun, L. M.; Susantyoko, R. A.; Zhang, Q. A hierarchical 3D carbon nanostructure for high areal capacity and flexible lithium ion batteries. *Carbon* **2016**, *98*, 504–509.
[235] Frackowiak, E.; Gautier, S.; Gaucher, H.; Bonnamy, S.; Beguin, F. Electrochemical storage of lithium in multiwalled carbon nanotubes. *Carbon* **1999**, *37*, 61–69.
[236] Wang, G. X.; Ahn, J. H.; Yao, J.; Lindsay, M.; Liu, H. K.; Dou, S. X. Preparation and characterization of carbon nanotubes for energy storage. *J. Power Sources* **2003**, *119–121*, 16–23.
[237] Claye, A. S.; Fischer, J. E.; Huffman, C. B.; Rinzler, A. G.; Smalley, R. E. Solid-state electrochemistry of the Li single wall carbon nanotube system. *J. Electrochem. Soc.* **2000**, *147*, 2845–2852.
[238] Gao, B.; Kleinhammes, A.; Tang, X. P.; Bower, C.; Fleming, L.; Wu, Y.; Zhou, O. Electrochemical intercalation of single-walled carbon nanotubes with lithium. *Chem. Phys. Lett.* **1999**, *307*, 153–157.
[239] Wang, W.; Ruiz, I.; Guo, S. R.; Favors, Z.; Bay, H. H.; Ozkan, M.; Ozkan, C. S. Hybrid carbon nanotube and graphene nanostructures for lithium ion battery anodes. *Nano Energy* **2014**, *3*, 113–118.
[240] Xu, J. M.; Han, Z.; Wu, J. S.; Song, K. X.; Wu, J.; Gao, H. F.; Mi, Y. H. Synthesis and electrochemical performance of vertical carbon nanotubes on few-layer graphene as an anode material for Li-ion batteries. *Mater. Chem. Phys.* **2018**, *205*, 359–365.
[241] Yitzhack, N.; Auinat, M.; Sezin, N.; Ein-Eli, Y. Carbon nanotube tissue as anode current collector for flexible Li-ion batteries—Understanding the controlling parameters influencing the electrochemical performance. *APL Mater.* **2018**, *6*, 111102.
[242] Adenusi, H.; Chass, G. A.; Passerini, S.; Tian, K. V.; Chen, G. H. Lithium batteries and the solid electrolyte interphase (SEI)—Progress and outlook. *Adv. Energy Mater.* **2023**, *13*, 2203307.
[243] Heiskanen, S. K.; Kim, J.; Lucht, B. L. Generation and evolution of the solid electrolyte interphase of lithium-ion batteries. *Joule* **2019**, *3*, 2322–2333.
[244] Wang, A. P.; Kadam, S.; Li, H.; Shi, S. Q.; Qi, Y. Review on modeling of the anode solid electrolyte interphase (SEI) for lithium-ion batteries. *npj Comput. Mater.* **2018**, *4*, 15.
[245] Peled, E.; Menkin, S. Review—SEI: Past, present, and future. *J. Electrochem. Soc.* **2017**, *164*, A1703–A1719.
[246] Ezzedine, M.; Zamfir, M. R.; Jardali, F.; Leveau, L.; Caristan, E.; Ersen, O.; Cojocaru, C. S.; Florea, I. Insight into the formation and stability of solid electrolyte interphase for nanostructured silicon-based anode electrodes used in Li-ion batteries. *ACS Appl. Mater. Interfaces* **2021**, *13*, 24734–24746.
[247] Arai, S.; Fukuoka, R. A carbon nanotube-reinforced noble tin anode structure for lithium-ion batteries. *J. Appl. Electrochem.* **2016**, *46*, 331–338.
[248] Chen, J. Z.; Zhang, L.; Gao, F.; Ren, M. X.; Hou, Y. L.; Zhao, D. L. Core–shell structured Si@Cu nanoparticles segregated in graphene-carbon nanotube networks enable high reversible capacity and rate capability of anode for lithium-ion batteries. *J. Electroanal. Chem.* **2023**, *943*, 117614.
[249] Wang, W.; Kumta, P. N. Nanostructured hybrid silicon/carbon nanotube heterostructures: Reversible high-capacity lithium-ion anodes. *ACS Nano* **2010**, *4*, 2233–2241.
[250] Sun, L.; Liu, Y. X.; Shao, R.; Wu, J.; Jiang, R. Y.; Jin, Z. Recent progress and future perspective on practical silicon anode-based lithium ion batteries. *Energy Storage Mater.* **2022**, *46*, 482–502.
[251] Xue, L. G.; Xu, G. J.; Li, Y.; Li, S. L.; Fu, K.; Shi, Q.; Zhang, X. W. Carbon-coated Si nanoparticles dispersed in carbon nanotube networks as anode material for lithium-ion batteries. *ACS Appl. Mater. Interfaces* **2013**, *5*, 21–25.
[252] Weng, W.; Lin, H. J.; Chen, X. L.; Ren, J.; Zhang, Z. T.; Qiu, L. B.; Guan, G. Z.; Peng, H. S. Flexible and stable lithium ion batteries based on three-dimensional aligned carbon nanotube/silicon hybrid electrodes. *J. Mater. Chem. A* **2014**, *2*, 9306–9312.
[253] Fu, K.; Yildiz, O.; Bhanushali, H.; Wang, Y. X.; Stano, K.; Xue, L. G.; Zhang, X. W.; Bradford, P. D. Aligned carbon nanotube-silicon sheets: A novel nano-architecture for flexible lithium ion battery electrodes. *Adv. Mater.* **2013**, *25*, 5109–5114.
[254] Yildiz, O.; Dirican, M.; Fang, X. M.; Fu, K.; Jia, H.; Stano, K.; Zhang, X. W.; Bradford, P. D. Hybrid carbon nanotube fabrics with sacrificial nanofibers for flexible high performance lithium-ion battery anodes. *J. Electrochem. Soc.* **2019**, *166*, A473–A479.
[255] Evanoff, K.; Khan, J.; Balandin, A. A.; Magasinski, A.; Ready, W. J.; Fuller, T. F.; Yushin, G. Towards ultrathick battery electrodes: Aligned carbon nanotube-enabled architecture. *Adv. Mater.* **2012**,

24, 533–537.
[256] Barrett, L. K.; Fan, J.; Laughlin, K.; Baird, S.; Harb, J. N.; Vanfleet, R. R.; Davis, R. C. Carbon monolith scaffolding for high volumetric capacity silicon Li-ion battery anodes. *J. Vac. Sci. Technol. B* **2017**, *35*, 041802.
[257] Fan, Y.; Zhang, Q.; Xiao, Q. Z.; Wang, X. H.; Huang, K. High performance lithium ion battery anodes based on carbon nanotube-silicon core–shell nanowires with controlled morphology. *Carbon* **2013**, *59*, 264–269.
[258] Epur, R.; Ramanathan, M.; Datta, M. K.; Hong, D. H.; Jampani, P. H.; Gattu, B.; Kumta, P. N. Scribable multi-walled carbon nanotube-silicon nanocomposites: A viable lithium-ion battery system. *Nanoscale* **2015**, *7*, 3504–3510.
[259] Fan, Y.; Zhang, Q.; Lu, C. X.; Xiao, Q. Z.; Wang, X. H.; Tay, B. K. High performance carbon nanotube-Si core–shell wires with a rationally structured core for lithium ion battery anodes. *Nanoscale* **2013**, *5*, 1503–1506.
[260] Harpak, N.; Davidi, G.; Melamed, Y.; Cohen, A.; Patolsky, F. Self-catalyzed vertically aligned carbon nanotube-silicon core–shell array for highly stable, high-capacity lithium-ion batteries. *Langmuir* **2020**, *36*, 889–896.
[261] Ho, D. N.; Yildiz, O.; Bradford, P.; Zhu, Y. T.; Fedkiw, P. S. A silicon-impregnated carbon nanotube mat as a lithium-ion cell anode. *J. Appl. Electrochem.* **2018**, *48*, 127–133.
[262] Gohier, A.; Laïk, B.; Kim, K. H.; Maurice, J. L.; Pereira-Ramos, J. P.; Cojocaru, C. S.; Van, P. T. High-rate capability silicon decorated vertically aligned carbon nanotubes for Li-ion batteries. *Adv. Mater.* **2012**, *24*, 2592–2597.
[263] Jessl, S.; Engelke, S.; Copic, D.; Baumberg, J. J.; De Volder, M. Anisotropic carbon nanotube structures with high aspect ratio nanopores for Li-ion battery anodes. *ACS Appl. Nano Mater.* **2021**, *4*, 6299–6305.
[264] Yoon, S.; Park, C. M.; Sohn, H. J. Electrochemical characterizations of germanium and carbon-coated germanium composite anode for lithium-ion batteries. *Electrochem. Solid-State Lett.* **2008**, *11*, A42–A45.
[265] Seo, M. H.; Park, M.; Lee, K. T.; Kim, K.; Kim, J.; Cho, J. High performance Ge nanowire anode sheathed with carbon for lithium rechargeable batteries. *Energy Environ. Sci.* **2011**, *4*, 425–428.
[266] Park, C. M.; Kim, J. H.; Kim, H.; Sohn, H. J. Li-alloy based anode materials for Li secondary batteries. *Chem. Soc. Rev.* **2010**, *39*, 3115–3141.
[267] Cui, G. L.; Gu, L.; Kaskhedikar, N.; Van Aken, P. A.; Maier, J. A novel germanium/carbon nanotubes nanocomposite for lithium storage material. *Electrochim. Acta* **2010**, *55*, 985–988.
[268] Susantyoko, R. A.; Wang, X. H.; Sun, L. M.; Pey, K. L.; Fitzgerald, E.; Zhang, Q. Germanium coated vertically-aligned multiwall carbon nanotubes as lithium-ion battery anodes. *Carbon* **2014**, *77*, 551–559.
[269] Gao, C. T.; Kim, N. D.; Salvatierra, R. V.; Lee, S. K.; Li, L. L.; Li, Y. W.; Sha, J.; Silva, G. A. L.; Fei, H. L.; Xie, E. Q. et al. Germanium on seamless graphene carbon nanotube hybrids for lithium ion anodes. *Carbon* **2017**, *123*, 433–439.
[270] Wang, X. H.; Susantyoko, R. A.; Fan, Y.; Sun, L. M.; Xiao, Q. Z.; Zhang, Q. Vertically aligned CNT-supported thick Ge films as high-performance 3D anodes for lithium ion batteries. *Small* **2014**, *10*, 2826–2829.
[271] Courtney, I. A.; Dahn, J. R. Electrochemical and *in situ* X-Ray diffraction studies of the reaction of lithium with Tin oxide composites. *J. Electrochem. Soc.* **1997**, *144*, 2045–2052.
[272] Kim, M. G.; Sim, S.; Cho, J. Novel core–shell Sn-Cu anodes for lithium rechargeable batteries prepared by a redox-transmetalation reaction. *Adv. Mater.* **2010**, *22*, 5154–5158.
[273] Sun, L. M.; Wang, X. H.; Susantyoko, R. A.; Zhang, Q. High performance binder-free Sn coated carbon nanotube array anode. *Carbon* **2015**, *82*, 282–287.
[274] Deng, W. N.; Chen, X. H.; Liu, Z.; Hu, A. P.; Tang, Q. L.; Li, Z.; Xiong, Y. N. Three-dimensional structure-based tin disulfide/vertically aligned carbon nanotube arrays composites as high-performance anode materials for lithium ion batteries. *J. Power Sources* **2015**, *277*, 131–138.
[275] Liu, X. M.; Huang, Z. D.; Oh, S. W.; Zhang, B.; Ma, P. C.; Yuen, M. M. F.; Kim, J. K. Carbon nanotube (CNT)-based composites as electrode material for rechargeable Li-ion batteries: A review. *Compos. Sci. Technol.* **2012**, *72*, 121–144.
[276] Mallakpour, S.; Khadem, E. Carbon nanotube-metal oxide nanocomposites: Fabrication, properties and applications. *Chem. Eng. J.* **2016**, *302*, 344–367.
[277] Zhao, Y.; Wang, L. P.; Sougrati, M. T.; Feng, Z. X.; Leconte, Y.; Fisher, A.; Srinivasan, M.; Xu, Z. C. A review on design strategies for carbon based metal oxides and sulfides nanocomposites for high performance Li and Na ion battery anodes. *Adv. Energy Mater.* **2017**, *7*, 1601424.
[278] Wu, Y.; Wang, J. P.; Jiang, K. L.; Fan, S. S. Applications of carbon nanotubes in high performance lithium ion batteries. *Front. Phys.* **2014**, *9*, 351–369.
[279] Seman, R. N. A. R.; Azam, M. A.; Mohamad, A. A. Systematic gap analysis of carbon nanotube-based lithium-ion batteries and electrochemical capacitors. *Renew. Sustain. Energy Rev.* **2017**, *75*, 644–659.
[280] Cao, K. Z.; Jin, T.; Yang, L.; Jiao, L. F. Recent progress in conversion reaction metal oxide anodes for Li-ion batteries. *Mater. Chem. Front.* **2017**, *1*, 2213–2242.
[281] Chen, Y.; Chen, X. Y.; Zhang, Y. L. A comprehensive review on metal-oxide nanocomposites for high-performance lithium-ion battery anodes. *Energy Fuels* **2021**, *35*, 6420–6442.
[282] Chen, J. S.; Lou, X. W. D. SnO_2-based nanomaterials: Synthesis and application in lithium-ion batteries. *Small* **2013**, *9*, 1877–1893.
[283] Sehrawat, P.; Julien, C.; Islam, S. S. Carbon nanotubes in Li-ion batteries: A review. *Mater. Sci. Eng. B* **2016**, *213*, 12–40.
[284] Zhu, K. L.; Luo, Y. F.; Zhao, F.; Hou, J. W.; Wang, X. W.; Ma, H.; Wu, H.; Zhang, Y. G.; Jiang, K. L.; Fan, S. S. et al. Free-standing, binder-free Titania/super-aligned carbon nanotube anodes for flexible and fast-charging Li-ion batteries. *ACS Sustainable Chem. Eng.* **2018**, *6*, 3426–3433.
[285] Pawlitzek, F.; Pampel, J.; Schmuck, M.; Althues, H.; Schumm, B.; Kaskel, S. High-power lithium ion batteries based on preorganized necklace type $Li_4Ti_5O_{12}$/VACNT Nano-composites. *J. Power Sources* **2016**, *325*, 1–6.
[286] Sun, L.; Kong, W. B.; Wu, H. C.; Wu, Y.; Wang, D. T.; Zhao, F.; Jiang, K. L.; Li, Q. Q.; Wang, J. P.; Fan, S. S. Mesoporous $Li_4Ti_5O_{12}$ nanoclusters anchored on super-aligned carbon nanotubes as high performance electrodes for lithium ion batteries. *Nanoscale* **2016**, *8*, 617–625.
[287] Wu, Y.; Wu, H. C.; Luo, S.; Wang, K.; Zhao, F.; Wei, Y.; Liu, P.; Jiang, K. L.; Wang, J. P.; Fan, S. S. Entrapping electrode materials within ultrathin carbon nanotube network for flexible thin film lithium ion batteries. *RSC Adv.* **2014**, *4*, 20010–20016.
[288] Ohzuku, T.; Ueda, A.; Yamamoto, N. Zero-strain insertion material of Li $[Li_{1/3}Ti_{5/3}]O_4$ for rechargeable lithium cells. *J. Electrochem. Soc.* **1995**, *142*, 1431–1435.
[289] Belharouak, I.; Koenig, G. M.; Amine, K. Electrochemistry and safety of $Li_4Ti_5O_{12}$ and graphite anodes paired with $LiMn_2O_4$ for hybrid electric vehicle Li-ion battery applications. *J. Power Sources* **2011**, *196*, 10344–10350.
[290] Yuan, T.; Yu, X.; Cai, R.; Zhou, Y. K.; Shao, Z. P. Synthesis of pristine and carbon-coated $Li_4Ti_5O_{12}$ and their low-temperature electrochemical performance. *J. Power Sources* **2010**, *195*, 4997–5004.
[291] Bach, S.; Pereira-Ramos, J. P.; Baffier, N. Electrochemical properties of sol-gel $Li_{4/3}Ti_{5/3}O_4$. *J. Power Sources* **1999**, *81–82*, 273–276.
[292] Lou, F. L.; Zhou, H. T.; Tran, T. D.; Buan, M. E. M.; Vullum-Bruer, F.; Rønning, M.; Walmsley, J. C.; Chen, D. Coaxial carbon/metal oxide/aligned carbon nanotube arrays as high-performance anodes for lithium ion batteries. *ChemSusChem* **2014**, *7*, 1335–1346.
[293] Luo, S.; Wu, H. C.; Wu, Y.; Jiang, K. L.; Wang, J. P.; Fan, S. S. Mn_3O_4 nanoparticles anchored on continuous carbon nanotube network as superior anodes for lithium ion batteries. *J. Power Sources* **2014**, *249*, 463–469.
[294] Li, Q.; Wu, Y. Q.; Wang, Z. M.; Ming, H.; Wang, W. X.; Yin, D.

M.; Wang, L. M.; Alshareef, H. N.; Ming, J. Carbon nanotubes coupled with metal ion diffusion layers stabilize oxide conversion reactions in high-voltage lithium-ion batteries. *ACS Appl. Mater. Interfaces* **2020**, *12*, 16276–16285.

[295] Jessl, S.; Copic, D.; Engelke, S.; Ahmad, S.; De Volder, M. Hydrothermal coating of patterned carbon nanotube forest for structured lithium-ion battery electrodes. *Small* **2019**, *15*, 1901201.

[296] Wu, Y.; Wei, Y.; Wang, J. P.; Jiang, K. L.; Fan, S. S. Conformal Fe_3O_4 sheath on aligned carbon nanotube scaffolds as high-performance anodes for lithium ion batteries. *Nano Lett.* **2013**, *13*, 818–823.

[297] Susantyoko, R. A.; Wang, X. H.; Xiao, Q. Z.; Fitzgerald, E.; Zhang, Q. Sputtered nickel oxide on vertically-aligned multiwall carbon nanotube arrays for lithium-ion batteries. *Carbon* **2014**, *68*, 619–627.

[298] Deng, W. N.; Chen, X. H.; Hu, A. P.; Zhang, S. Y. Graphitic carbon-wrapped NiO embedded three dimensional nitrogen doped aligned carbon nanotube arrays with long cycle life for lithium ion batteries. *RSC Adv.* **2018**, *8*, 28440–28446.

[299] He, X. F.; Wu, Y.; Zhao, F.; Wang, J. P.; Jiang, K. L.; Fan, S. S. Enhanced rate capabilities of Co_3O_4/carbon nanotube anodes for lithium ion battery applications. *J. Mater. Chem. A.* **2013**, *1*, 11121–11125.

[300] Liu, W. W.; Lu, C. X.; Liang, K.; Tay, B. K. A high-performance anode material for Li-ion batteries based on a vertically aligned CNTs/$NiCo_2O_4$ core/shell structure. *Part. Part. Syst. Charact.* **2014**, *31*, 1151–1157.

[301] Zhu, K. L.; Li, C. Y.; Jiao, Y. S.; Zhu, J. W.; Ren, H. T.; Luo, Y. F.; Fan, S. S.; Liu, K. Free-standing hybrid films comprising of ultra-dispersed Titania nanocrystals and hierarchical conductive network for excellent high rate performance of lithium storage. *Nano Res.* **2021**, *14*, 2301–2308.

[302] Park, M.; Zhang, X. C.; Chung, M.; Less, G. B.; Sastry, A. M. A review of conduction phenomena in Li-ion batteries. *J. Power Sources* **2010**, *195*, 7904–7929.

[303] Pawlitzek, F.; Althues, H.; Schumm, B.; Kaskel, S. Nanostructured networks for energy storage: Vertically aligned carbon nanotubes (VACNT) as current collectors for high-power $Li_4Ti_5O_{12}$ (LTO)//$LiMn_2O_4$ (LMO) lithium-ion batteries. *Batteries* **2017**, *3*, 37.

[304] Ning, G. Q.; Zhang, S. C.; Xiao, Z. H.; Wang, H. B.; Ma, X. L. Efficient conductive networks constructed from ultra-low concentration carbon nanotube suspension for Li ion battery cathodes. *Carbon* **2018**, *132*, 323–328.

[305] Yilmaz, M.; Raina, S.; Hsu, S. H.; Kang, W. P. Micropatterned arrays of vertically-aligned CNTs grown on aluminum as a new cathode platform for $LiFePO_4$ integration in lithium-ion batteries. *Ionics* **2019**, *25*, 421–427.

[306] Luo, S.; Wang, K.; Wang, J. P.; Jiang, K. L.; Li, Q. Q.; Fan, S. S. Binder-free $LiCoO_2$/carbon nanotube cathodes for high-performance lithium ion batteries. *Adv. Mater.* **2012**, *24*, 2294–2298.

Table of contents

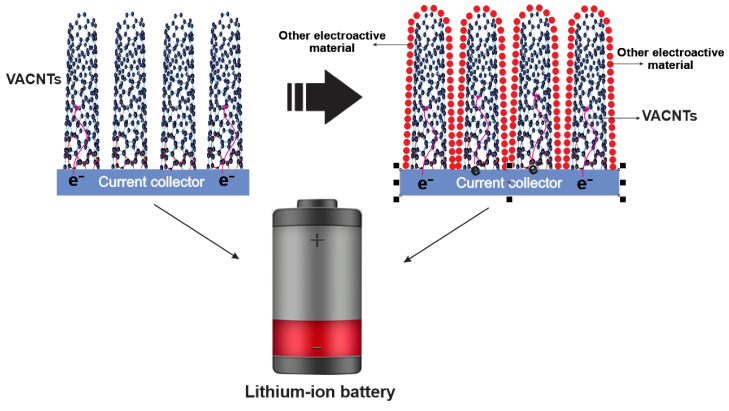

Vertically aligned carbon nanotubes (VACNTs) offer superior electrochemical performance in lithium-ion batteries (LIBs) owing to their unique properties. Their well-defined vertical channels facilitate fast electronic transport and ion diffusion.